water

MDPI

Article

Hydrogeochemical and Isotopic Characteristics of the Hot Springs in the Litang Fault Zone, Southeast Qinghai–Tibet Plateau

Rui Zhou, Xiaocheng Zhou *, Ying Li *, Miao He, Jingchao Li, Jinyuan Dong, Jiao Tian, Kaiyue Li, Yucong Yan, Shupei Ouyang, Fengli Liu and Zhixin Luo

CEA Key Laboratory of Earthquake Prediction (Institute of Earthquake Forecasting), China Earthquake Administration, Beijing 100036, China; cnuarui@sina.com (R.Z.); IEFhemiao@163.com (M.H.); lijc@ief.ac.cn (J.L.); dongjinyuan@163.com (J.D.); tianjiao375@163.com (J.T.); lky@ief.ac.cn (K.L.); yanyucong2020@163.com (Y.Y.); ouyangshupei888@163.com (S.O.); liufengli9723@163.com (F.L.); lzxxg0127@163.com (Z.L.)

* Correspondence: zhouxiaocheng188@163.com (X.Z.); subduction6@hotmail.com (Y.L.)

Abstract: Based on the observation of the geochemical characteristics of 19 hot springs in the Litang Fault Zone (LFZ) from 2010 to 2019, the major elements, trace elements, and stable isotopes were investigated, and a conceptual model of ground fluid circulation in the LFZ was established. The main hydrochemical type of hot spring water samples is HCO_3^--Na^+. The δ^2H values range from −157.6‰ to −123.4‰ and $\delta^{18}O$ values range from −24.5‰ to −15.4‰. The hot spring water in the Litang fault zone is mainly recharged by infiltrating precipitation, with a recharge elevation of 4062~6018 m. Hydrochemical types of Litang hot springs are mainly controlled by the circulation of groundwater in a deep fault system, and are related to the rock lithology of thermal reservoir and water–rock reaction areas. Hot springs in the Litang fault zone attribute to three different heat sources, belonging to three geothermal systems. The flow direction of groundwater in the LFZ is roughly from northwest to southeast along the Litang fault. The deeper the circulation depth of hot spring water on the fault, the higher the thermal reservoir temperature and the stronger the seismic activity of the segment, which is closely related to the increase in pore fluid pressure, rock weakening, and deep fluid upwelling. This study is helpful for further study on regional hydrogeological environments and provides a scientific basis for revealing geothermal fluid movement in fault zones.

Keywords: hot spring; hydrogeochemistry; stable isotopes; geothermometer; circulation; the Litang fault; earthquake

Citation: Zhou, R.; Zhou, X.; Li, Y.; He, M.; Li, J.; Dong, J.; Tian, J.; Li, K.; Yan, Y.; Ouyang, S.; et al. Hydrogeochemical and Isotopic Characteristics of the Hot Springs in the Litang Fault Zone, Southeast Qinghai–Tibet Plateau. *Water* **2022**, *14*, 1496. https://doi.org/10.3390/w14091496

Academic Editor: Maurizio Barbieri

Received: 3 April 2022
Accepted: 3 May 2022
Published: 6 May 2022

1. Introduction

The hydrogeological properties of hot springs in a fault zone contain abundant information regarding the origin of geothermal fluids and the flow process of underground fluids; therefore, the application of hydrogeochemistry of geothermal water along fault segments provides an effective way to understand the heat source, thermal groundwater circulation, and material migration in the Earth's lithosphere [1,2]. In China, the heat flow values have a decreasing trend from the Qinghai–Tibet Plateau to the Sichuan Basin [3]. The regional geothermal anomalies distribution in the southeastern margin of the Qinghai–Tibet Plateau are very obvious. The high value of heat flow in western Sichuan is distributed along the Dege–Xiangcheng fault, the Ganzi–Litang fault, and Kangding. Many hot springs are distributed in fault zones in western Sichuan, China, such as Litang, Xiangcheng, and Ganzi. These hydrothermal active areas are distributed with the development of fault zones [4]. The middle-high temperature springs in the abovementioned fault zones have made the eastern Qinghai–Tibet Plateau geothermal belt as a research hotspot of hydrogeology.

Previous studies have reported hydrogeochemical characteristics and evolution of hot springs in eastern Qinghai–Tibet Plateau geothermal belt [5], the gas and fluid geochemistry of the hot springs in the Litang fault zone [6,7], the geochemistry of the thermal springs in Batang geothermal field [8], and the hydrochemical characteristics of hot spring water in Kangding [9,10]. Nevertheless, the heat source, hydrogeochemical characteristics and groundwater circulation of hot springs in the eastern Qinghai–Tibet Plateau geothermal belt, and the related flow path of underground geothermal water are still unclear [11,12]. Moreover, the step between the highest peak of the Longmen Shan thrust belt and Sichuan Basin in terrain topography to some extent marks the boundary between the seismically active Qinghai–Tibet Plateau and the tectonically stable Ordos block, Sichuan Basin, and South China block [13]. This transitional area is also known as the NS-trending tectonic zone or the NS seismic belt due to its high tectonic activity [13–15]. The phenomenon that the changes of hydrogeochemical characteristics of hot spring water related to large near-field earthquakes had been observed in the Xianshuihe fault zone [10]. Zhou et al. [6] studied the gas geochemical characteristics of hot springs in the Litang fault zone, the results show that R_C/R_A ratio (air corrected He isotope ratio) and $\delta^{13}C_{CO_2}$ values have some changes after the 2013 Lushan M_s7.0 earthquake and the 2014 Kangding M_s6.3 earthquake, indicating that the earthquake has changed the regional tectonic environment. However, research on the hydrogeochemical characteristics of hot springs in the Litang fault zone, especially the relationship between hot springs distributed along the fault zone and seismic activity of the fault zone, is not sufficient.

The aim of the present study is to obtain the hydrogeochemical characteristics of hot spring water in the Litang fault zone, and to establish a conceptual model to discuss the process of ground fluid circulation, and the relationship between ground fluid circulation and earthquakes occurred in the fault zone.

2. Seismogeological Setting

Tectonostratigraphically, four structural domains across the Yidun Arc region are the western Songpan–Ganzi Fold Belt, the eastern Yidun terrane, the western Yidun terrane, and the eastern Qiangtang terrane (Figure 1a,b) [16,17]. The Yidun terrane is located between the Qiangtang and Songpan–Ganzi terranes, which is separated by two Paleo-Tethys oceanic subduction zones, with the Ganzi–Litang suture to the east and the Jinshajiang suture to the west [6,7,18]. The western Yidun terrane, also referred to Zhongza Massif, is composed of metamorphosed Paleozoic marine sediments, and is comparable Paleozoic passive margin stratigraphy of the western Yangtze Block, which can be considered as a micro-continent block split the western Yangtze Block in the Late Permian. Sediment is metamorphic Paleozoic carbonates, clastic rocks, and intercalated mafic volcanogenics. The eastern Yidun terrane is dominated by a Triassic volcanic-flysch sequence, the Yidun Group, and Late Triassic arc-related plutons. The Middle to Late Triassic volcanosedimentary successions is composed of flysch and mafic to felsic volcanic rocks of an arc complex, which formed by the westward subduction of the Ganzi–Litang oceanic lithosphere [16,19–21]. The Middle and Lower Triassic strata are shale and sandstone without volcanic rocks with some limestone, which are overlying by the unconformity of the Upper Triassic strata. At the bottom of the Upper Triassic, the strata are basaltic volcanic rocks, the lithological association changes in sequence as limestone intercalated with basaltic volcanic rocks, sandstone and shale, intermediate and acidic volcanic rocks intercalated with sandstone and shale with a small amount of limestone, and the uppermost transition to non-marine coal-bearing strata [22]. The Northern Yidun terrane was relatively extended at ~ 235–230 Ma, i.e., the steep-angle subduction, which resulted in easy access of melts from the convective mantle wedge and forming a range of volcanic rocks. The continuous westward subduction of the Ganzi–Litang oceanic plate resulted in the rifting and opening of the Northern Yidun terrane back arc basin. In the back-arc basin, decompression melting caused by upwelling of asthenosphere may be the reason for mafic magmas emplacement. These mafic magmas underplated the ancient lower crust of northern Yidun terrane and

triggered anatexis, resulting in a series of magmatism from mafic to felsic. At the end of the Triassic (225–215 Ma), the Ganzi–Litang ocean closed, leading to the collision of the Yidun terrane and the Songpan–Ganzi Fold Belt. The slab pull of descending and remnant Litang–Ganzi oceanic lithosphere caused breakoff of the slab, resulting in the upwelling of the asthenosphere beneath the young collision zone. The convection provided by upwelling asthenosphere may have resulted in partial melting of the crust of Northern Yidun terrane paleocontinent crust and the emplacement of post-collision granite along the east of northern Yidun terrane [23–25]. The Yidun terrane is characterized by two phases of Mesozoic magmatism, one stage is in Late Triassic [26], and the other is in Late Cretaceous [27]. The Late Triassic magmatism is most intense in the Yidun terrane, including volcanic and intrusive rocks. Volcanics are widely distributed in the whole Yidun terrane, include basalt, andesite, dacite, and rhyolite. Intrusive rocks are mainly granitoids with a small amount of intermediate and mafic magmatic rocks [22].

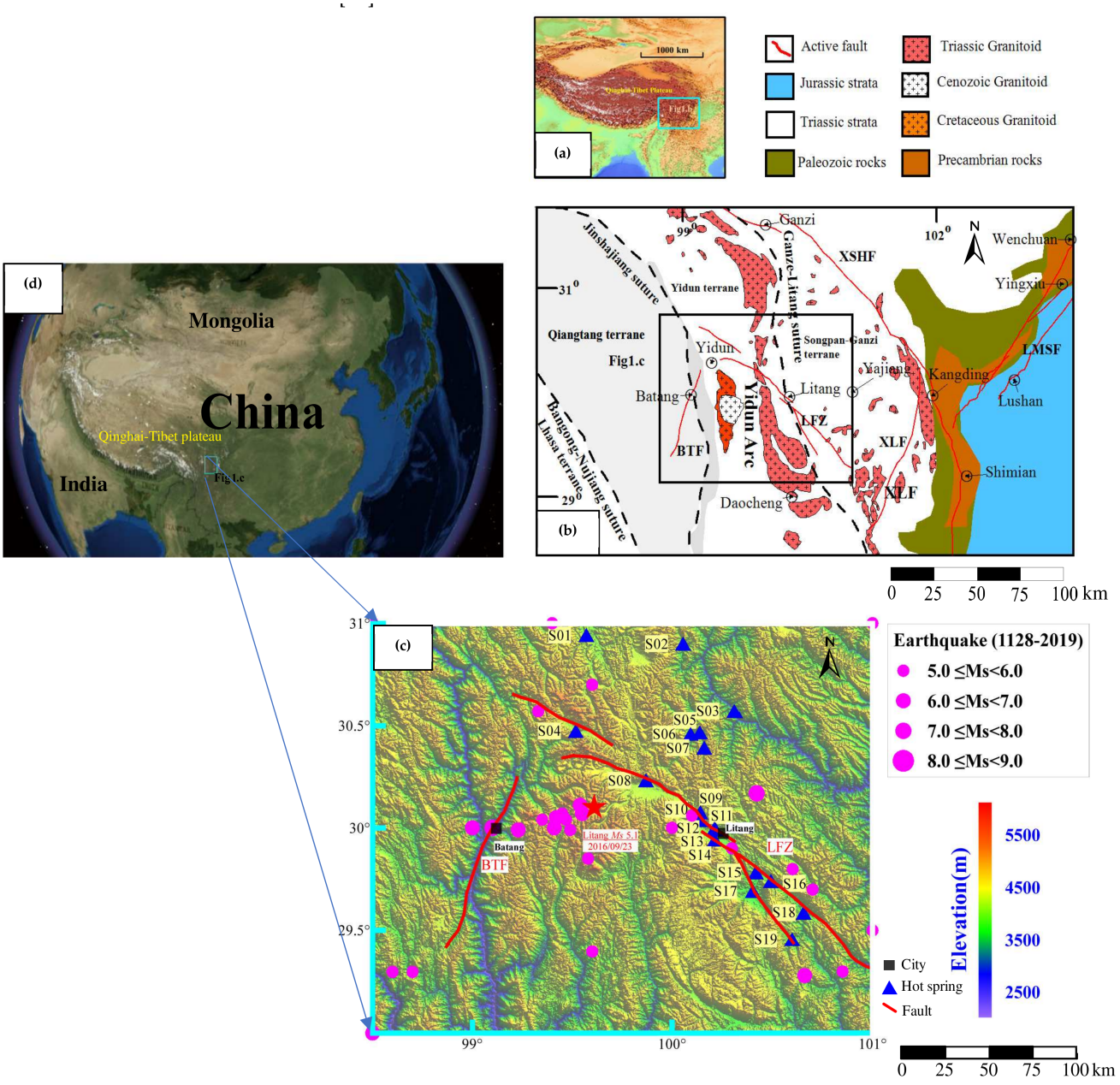

Figure 1. Topographic, geological map, global figure of the study area, and location of water sampling sites of the hot spring along the Litang fault zone (Modified from [6]). (**a**) Topographic map of the Qinghai–Tibet

Plateau. (**b**) Generalized geological map of the study area. The box in (**a**). Abbreviations: LFZ—Litang fault zone, XSHF—Xianshuihe fault, LMSF—Longmenshan fault, BTF—Batang fault, XLF—Xiaojinhe-Lijiang fault. (**c**) Location of water sampling sites of the hot spring along the LFZ. The boxes in (**b**) and (**d**). (**d**) Global figure. Red star represents as the 2016 Litang M_S 5.1 earthquake.

The Litang fault zone (LFZ) is an important active fault within the northwestern Sichuan subblock. Together with the Ganzi–Yushu, Xianshuihe, and Anninghe fault zones on its northern, eastern and southeastern sides. The LFZ constitutes the lateral extrusion tectonic system in the southeastern part of the Qinghai–Tibet Plateau [28]. The NW-striking LFZ is mostly parallel to the highly active Xianshuihe fault (XSHF), with both faults veering toward a southerly strike to SE. The LFZ is a transtensive left-lateral fault system, which consists of several NW-SE fault segments running for ~190 km parallels to the XSHF, then progressively turning N-S [29]. The LFZ consists of four right-stepping en-echelon left-lateral/normal subordinate faults, and these are Cuopu, Maoya, Litang, and South Jawa–Dewu faults, respectively [13]. The fault segments are all dominated by left-lateral strike-slip with a reverse dip–slip component [6]. LFZ is located within high altitude (4000~4500 m a.s.l.) and low-relief Litang Plateau in the northwest of Sichuan Province, and is ~190 km long and ~25 km wide with discontinuous distribution. The maximum elevation of the mountain ranges decreases from NW to SE, from ~5800 m near Cuopu, where the range rises ~1700 m above the mean elevation of the plateau, to ~5000 m near Maoya and Litang, where the ranges rise ~1000 m above the plateau [29].

The LFZ is very tectonically active, and three historical $7 < M < 7.5$ earthquakes occurred in this fault system since 1700. The last large earthquake of Maoya segment occurred in 1886 (M_S7.1). The 1948 M_S7.3 earthquake in the LFZ had at least ruptured South Jawa–Dewu segment with ~41 km of surface ruptures. The latest earthquake along the Litang segment occurred in 1890 (M_S7.1) with ~50 km surface rupture. Most recently, an M_S5.1 earthquake occurred on Sept 23, 2016, in the LFZ, China (Figure 1c,d) [6,28].

3. Sampling and Methods

3.1. Sampling

A total of 49 hot spring water samples distributed in 19 sites were collected in the LFZ in June 2010, May 2013, March 2015, April 2016, June 2017, July 2018, and June 2019, respectively. The sampling locations (Sampling site: Qiyu, Tongxiao, Maxi, Zhangke, Beiluexi, Juewu, Luexi, Heni, Qukailong, Daoban, Maoya 1, Maoya 2, MYS, Maohe, Jiawa, Shangmula, Chaka, Xiamula, and Dewu; Sampling ID: S01, S02, S03, S04, S05, S06, S07, S08, S09, S10, S11, S12, S13, S14, S15, S16, S17, S18, and S19) numbered from north to south are shown in Figure 1c (Supplementary Table S1). For example, S13 represents not only the position of MYS sampling site, but also the MYS spring. When there are multiple data points for one sampling ID in the diagram used in this investigation, using sampling ID to represent the water sample from a spring, it does not refer to a specific sample, but the general characteristics of that spring water, and each point represents a specific sample. If there is only one point, it shows that only one sample can be used in the specific measurement, then the measurement result of the specific sample is used to characterize the properties of the spring. If there is a number followed by ID, such as S13-2, which refers to the sample collected in MYS spring in the second round. In 2010–2019, spring water was sampled seven times from S08 and S13 sites; sampled five times from S17 site; sampled four times from S10 site; sampled three times from S04, S09, S14, and S15 sites; sampled twice from S16, S18, and S19 sites; and the water of the remaining spring sites was sampled once. Hot spring samples for trace element measurements on the fault were collected in 2010, 2017, and 2018, respectively (Supplementary Table S2). The springs sampled more than one time are the hot springs on the fault zone; those sampled only once are considered as the background of the fault zone. The samples were collected from the LFZ for strontium isotopes measurements in 2017.

The samples were collected after filtration through a 0.45 μm membrane. All hot spring samples were kept in polyethylene bottles for laboratory analysis [30]. The hot spring water sample were collected for the determination of major element concentrations, the isotopes of hydrogen and oxygen, SiO_2 concentration, and strontium isotopes. Polyethylene bottles used for sampling had been immersed in ultrapure water for 3 days, then vibrated by ultrasonic vibration machine for 15 min, rinsed with ultrapure water, and then dried in the oven. The bottles had been carefully prewashed 3~5 times with the hot spring water at each sampling point before collecting each sampling. The polyethylene bottle was completely immersed in water during sampling, and the air in the bottle was cleaned to avoid the impact of the chemical components of air on the water sample. Prior to field sample collection, temperature, pH, and electrical conductivity of hot spring water were measured in situ with handheld meters calibrated prior to sampling (Supplementary Table S1), and 1.00 mL of concentrated nitric acid (pH < 2) was added to the sample for the measurement of trace elements, which was stored at room temperature.

3.2. Methods

The spring water temperatures were measured in the field with a Hengxin (AZ 8821) digital thermometer with an error of 0.15 °C [9]. The measurement of major-element (cation: K^+, Na^+, Mg^{2+}, and Ca^{2+}; anion: Cl^-, Br^-, $NO_3{}^-$, and $SO_4{}^{2-}$) in hot spring water samples was completed by ion chromatograph in the Key Laboratory of Earthquake Prediction, China Earthquake Administration. The instrument was Dionex ICS-900 ion chromatograph and AS40 automatic sampler, and the detection limit was 0.01 mg/L. The concentrations of $HCO_3{}^-$ and $CO_3{}^{2-}$ in hot spring water were measured by ZDJ-3D potentiometric titrator through standard titration procedure, and the concentration of hydrochloric acid with 0.1% methyl orange and 1% phenolphthalein (reproducibility within 2%) used for titration was 0.05 mol/L.

The trace elements of samples were analyzed by element-type inductively coupled plasma mass spectrometer (ICP-MS) in Beijing Research Institute of Uranium Geology, and the accuracy of the analysis was better than 5%. The hydrogen and oxygen isotopes were determined by gas mass spectrometer MAT253, and an international standard, specifically the Vienna Standard Mean Ocean Water (V-SMOW), was invoked as the standard, which was denoted as δ^2H and $\delta^{18}O$, respectively. Hydrogen and oxygen isotope reference materials were the international standard (GBW04401, 04402). Analysis accuracy of the samples was $\delta^2H < 1‰$ and $\delta^{18}O < 0.2‰$. The SiO_2 concentration was determined by inductively coupled plasma emission spectrometer Optima-5300 DV. Sr element was measured by Element XR ICP-MS from the Test Center of the Beijing Research Institute of Uranium Geology.

3.3. Data Processing

The detected cation concentrations were Li^+, Na^+, K^+, Mg^{2+}, and Ca^{2+}, and the anion concentrations were F^-, Cl^-, Br^-, $NO_3{}^-$, and $SO_4{}^{2-}$. In order to calibrate the chromatography, the standard sample should be measured before measuring each batch of water samples, and the measurement deviation is within 2‰. The ion balance (*ib*) is calculated based on the equation:

$$ib(\%) = \frac{\sum cations - \sum anions}{0.5(\sum cations + \sum anions)} \times 100 \quad (1)$$

The results of major ions of spring water are regarded to be acceptable for analyzing the hydrogeochemical characteristics when the balance error between anions and cations was within ±5% [9,31].

The equation of groundwater recharge elevation can be expressed as

$$H = \frac{\delta_S - \delta_P}{K} + h \quad (2)$$

where H is the recharge area elevation (m), h is the spring elevation, δ_S is the isotope composition of groundwater, δ_P is the isotope composition of precipitation near sampling site, and K is the isotope elevation gradient (‰/100 m). Specifically for hydrogen and oxygen, this equation can be transformed into [32].

$$H_{2\mathrm{H}} = \frac{\delta^2\mathrm{H}_S - \delta^2\mathrm{H}_P}{K_\mathrm{D}} + h \tag{3}$$

$$H_\mathrm{O} = \frac{\delta^{18}\mathrm{O}_S - \delta^{18}\mathrm{O}_P}{K_\mathrm{O}} + h \tag{4}$$

Online Isotopes Precipitation Calculation (OIPC, version 3.1) was used to calculate the average value of hydrogen and oxygen isotopes at the sampling site. Data obtained by OIPC 3.1 were derived from the Global Network of Isotopes in Precipitation (GNIP) established by the International Atomic Energy Agency (IAEA) and World Meteorological Organization (WMO).

The chloro-alkaline indices (CAI) can be used to determine whether cation cross-adsorption process occurs in groundwater. As is shown in Equations (5) and (6), all values are expressed in meq·L^{-1}. If both CAI 1 and CAI 2 are negative values, it indicates that magnesium and calcium from water are exchanged with sodium and potassium in rock. Conversely, a positive ratio of CAI signifies the reverse direction exchange [33].

$$\mathrm{CAI\ 1} = \frac{\left[\mathrm{Cl}^- - \left(\mathrm{Na}^+ + \mathrm{K}^+\right)\right]}{\mathrm{Cl}^-} \times 100\% \tag{5}$$

$$\mathrm{CAI\ 2} = \frac{\left[\mathrm{Cl}^- - \left(\mathrm{Na}^+ + \mathrm{K}^+\right)\right]}{\mathrm{HCO}_3^- + \mathrm{SO}_4^{2-} + \mathrm{NO}_3^- + \mathrm{CO}_3^{2-}} \times 100\% \tag{6}$$

The saturation indices (SI) of the hot spring water at outlet temperature and pH in the LFZ calculated with PHREEQC software using the PHREEQC database are listed in Supplementary Table S3. In order to further distinguish ordered and disordered dolomite, PHREEQC software was used to calculate SI of dolomite and calcite with LLNL thermodynamic database. The SiO_2 and cationic geothermometers were used to calculate reservoir temperatures.

Enrichment factor analysis is an essential method for judging and evaluating the enrichment degree and source of elements. The calculation equation of enrichment factor can be written as

$$EF_i = (C_i/C_R)_\mathrm{w}/(C_i/C_R)_\mathrm{r} \tag{7}$$

where C_R is the selected reference element content, C_i is the element content in the sample, "w" means the element concentration in the water sample, and "r" means the element concentration in the rock.

The Origin 2021b, Surfer 17.1, and Grapher 17.3 software were used to perform plots and Voxler 4.2 was used to build the conceptual model of ground fluid circulation in the LFZ.

4. Results

4.1. Hydrogeochemical Characteristics

The field measured parameters, stable isotopes, and concentrations of major ions of all water samples are given in Supplementary Table S1. The temperature of hot spring water varies from 28.4 °C to 87.0 °C, and the mean temperature of 49 hot spring samples is 53.6 °C (Supplementary Table S1, Figure 2). The electrical conductivity (Cond.) of hot springs ranges from 3.13 μs/cm to 68,500 μs/cm, and the median is 2070 μs/cm. The pH values of hot spring samples range from 6.68 to 9.78. The pH values of nine spring water samples are lower than 7.0, while the other water samples are higher than 7.0. The calculated total dissolved solids (TDS) of water varies from 163.4 mg/L to 2021.7 mg/L,

and the mean is 1274.7 mg/L. All hot spring water samples are fresh water and brackish water. The TDS of water samples (S14-1, S14-2, S14-3) collected in S14 site was significantly lower than that of other hot springs. Silica concentrations in the spring water samples are slightly low, ranging from 17.6 mg/L to 72.4 mg/L. The silica concentration of S04-2 sample is relatively high, which is 72.4 mg/L.

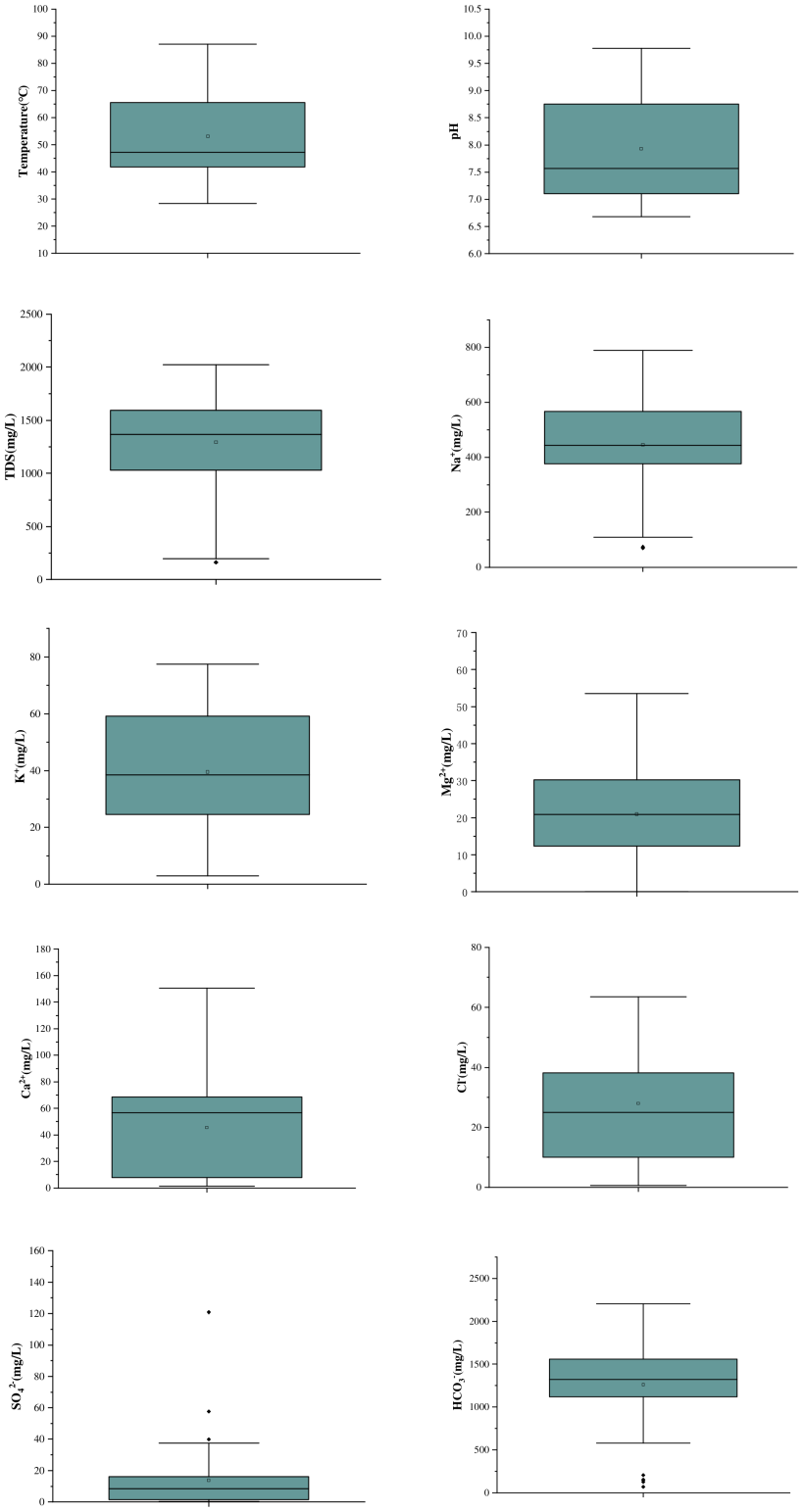

Figure 2. *Cont.*

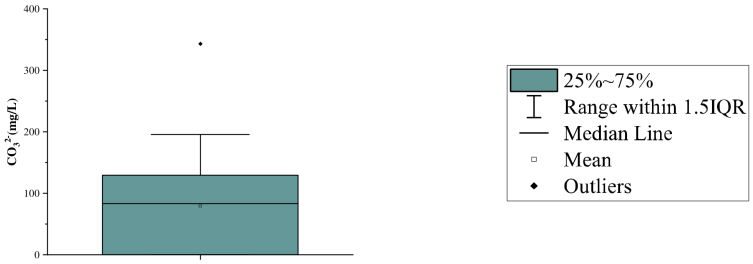

Figure 2. The box plots of temperature; pH; TDS; and Na^+, K^+, Mg^{2+}, Ca^{2+}, Cl^-, $SO_4{}^{2-}$, $HCO_3{}^-$, and $CO_3{}^{2-}$ concentrations of water samples collected in LFZ.

Except for samples of S01, S09-1, and S17-2, the hydrochemical type of hot spring water samples is $HCO_3{}^-$-Na^+. The hydrochemical types of S01, S09-1, and S17-2 samples are $HCO_3{}^-$-Na^+·Ca^{2+}, $HCO_3{}^-$-Na^+·Ca^{2+}, and $HCO_3{}^-$·Cl^--Na^+, respectively. The main cations of hot spring water in the LFZ are Na^+, K^+, Ca^{2+}, and Mg^{2+}. The Na^+ concentrations range from 69.7 mg/L to 789.2 mg/L, and the mean of Na^+ concentrations is 439.4 mg/L. Some major ion concentrations vary greatly, such as Ca^{2+} (1.4~150.5 mg/L) and Mg^{2+} (0~53.5 mg/L). The main anion of the hot spring water samples in LZF is $HCO_3{}^-$, which ranges from 69.5 mg/L to 2205.8 mg/L. The average concentration of $HCO_3{}^-$ is 1241.1 mg/L. Apart from S10-2 and S18-1 samples, which have no $SO_4{}^{2-}$ anion, the $SO_4{}^{2-}$ concentration of different hot spring water samples ranges from 0.2 mg/L to 120.9 mg/L, and the average is 14.1 mg/L. Although the variation range of Cl^- in samples is relatively larger, all samples have chloride ion, which ranges from 0.7 mg/L to 63.5 mg/L. Besides the above major ions, the major anions of LFZ water samples are $NO_3{}^-$ and Br^-, and only one sample detected Br^-. For the hot spring water samples collected in the LFZ, quite a few samples have a certain amount of Li^+ and F^-, and the average concentrations are 1.8 mg/L and 4.8 mg/L, respectively.

4.2. Oxygen and Hydrogen Isotopes

The hot spring water has δ^2H values ranging from −157.6‰ to −123.4‰ and $\delta^{18}O$ values ranging from −24.5‰ to −15.4‰. Except for the S04 site, the S01~S07 sites have a certain distance to the Litang fault, and are situated in the north of the study area. The samples collected from these sites have similar δ^2H values, ranging from −133.9‰ to −123.4‰, and the $\delta^{18}O$ values are in the range of −17.5‰ to −15.4‰. The average of δ^2H values and $\delta^{18}O$ values is −127.8‰ and −16.1‰. Commonly, in the southeast part of the study area, the hydrogen and oxygen isotopes of some sampling points in the Litang fault zone are slightly lower, with δ^2H values ranging from −157.6‰ to −126.6‰ and $\delta^{18}O$ values ranging from −24.5‰ to −15.9‰. The average of δ^2H values and $\delta^{18}O$ values are −148.1‰ and −19.7‰. The S06 sample has the highest oxygen and hydrogen isotopic composition ($\delta^{18}O$ = −15.4‰ and δ^2H = −123.4‰).

5. Discussion

5.1. Origin of Spring Water

Hydrogen and oxygen stable isotopes can be used to identify the origin of spring water. Craig (1961) studied the hydrogen and oxygen isotopes of water samples from rivers, lakes, and precipitation worldwide, and established the exact nature of the isotopic relationship in meteoric water, which can be expressed as $\delta^2H = 8 \times \delta^{18}O + 10$, namely global meteoric water line (GMWL) [34]. The $\delta^{18}O$ values of river water across the Qinghai–Tibet Plateau range between −20.8‰ and −3.4‰, and the δ^2H values range between −165‰ and −19‰. The local meteoric water line (LMWL) of river water in the Qinghai–Tibet Plateau is $\delta^2H = 8.6 \times \delta^{18}O + 16.5$. The local lake water line (LLWL) of the Qinghai–Tibet Plateau is $\delta^2H = 6.4 \times \delta^{18}O - 24.4$ [35]. The local lake water line (LLWL) of the Qinghai–Tibet Plateau is built by 111 lake water samples collected from the Qinghai–Tibet Plateau. The

geographical coordinates of these data range from 29.1°N to 33.5°N and from 79.8°E to 103.4°E. As is shown in Figure 3, the S02, S04, S05, S06, S07, S08, S09, S10, S13, S17, S18, and S19 hot springs deviate the LMWL, while the S01, S03, S15, and S16 hot springs are on the LMWL. The points of hot spring water located around local meteoric water line (LLWL), suggesting that the hot spring water is of meteoric origin. The recharge water is heated to hot water by heating source in deep circulation. In addition, most of the sample points located on the local lake water line (LLWL), indicating that hot spring water has homology with lake water in origin to some extent. The hot spring water whose $\delta^{18}O$ value deviated from the local meteoric water line and inclined to the higher $\delta^{18}O$ value, due to the isotopic exchange of ^{18}O with rock that came into contact with the water [36,37].

The altitude effect means the change in the stable isotopic composition of precipitation with elevation [38]. Isotopic composition of oxygen and hydrogen decrease with the increase in precipitation elevation because heavy isotopes loss gradually. This effect can be utilized to calculate the recharge elevation of groundwater. The oxygen-18 shifts often occur in high-temperature geothermal fields; therefore, the result of recharge elevation deduced from deuterium elevation effect is more accurate than that from oxygen [31,39]. However, due to a previous report of $\delta^{18}O$ elevation gradient for precipitation in the southeastern margin of the Qinghai–Tibet Plateau, the involved region is closer to the study area, and as a result oxygen isotope also can be attempted to elucidate the recharge elevation. The calculated data take into consideration the water vapor transport process, geographical location, temperature, and other factors [40–42]. The $\delta^{2}H$ elevation gradient in the Qinghai–Tibet Plateau is −2.4‰/100 m [31]. The $\delta^{18}O$ elevation gradient for monsoon season and non-monsoon season are −0.27‰/100 m and −0.32‰/100 m [43], and the average value −0.295‰/100 m is taken as K_O to calculate the recharge elevation. As is presented in Table 1, $\delta^{18}O$ and $\delta^{2}H$ are the isotope compositions of groundwater, $\delta^{18}O^{*}$ and $\delta^{2}H^{*}$ are the isotope compositions of precipitation near sampling site computed by Online Isotopes Precipitation Calculation (OIPC), the recharge elevation calculated with Equation (3) by hydrogen isotope is 4518~6174 m, and calculated with Equation (4) by oxygen isotope is 4062~6018 m.

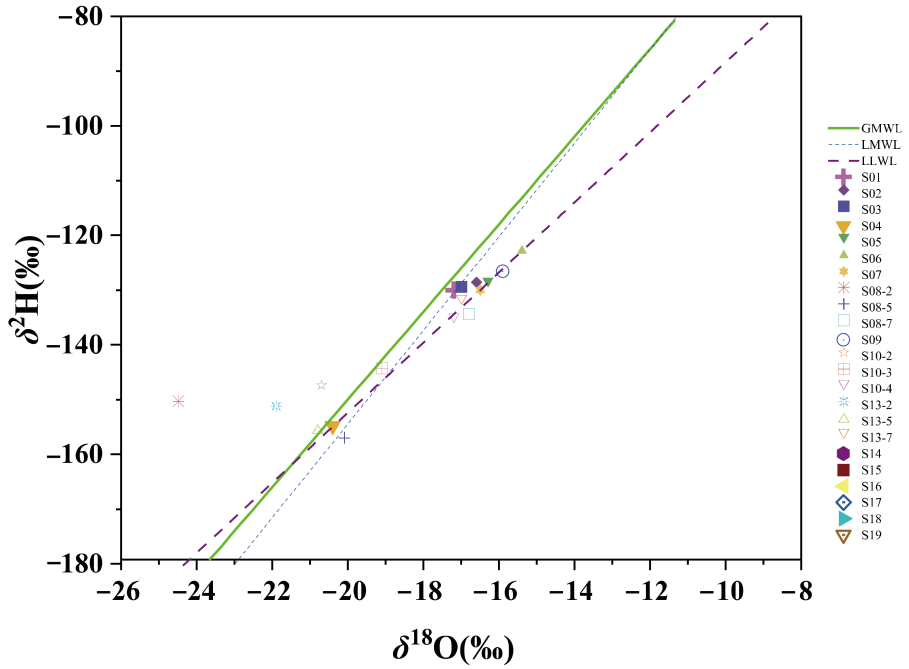

Figure 3. Scatter plot of the $\delta^{2}H$ and $\delta^{18}O$ values.

Table 1. The recharge elevation calculation of hot spring waters in the LFZ.

Sampling ID	$\delta^{18}O$(‰)	$\delta^{2}H$(‰)	$\delta^{18}O^{*}$(‰)	$\delta^{2}H^{*}$(‰)	H_{2H}(m)	H_O (m)
S01	−17.2	−130.0	−14.6	−105	4798	4814
S02	−16.6	−129.2	−14.1	−102	4902	4616
S03	−17.0	−130.0	−12.1	−87	4660	4529
S04	−20.4	−154.8	−15.3	−110	5953	5815
S05	−16.3	−129.3	−14.0	−100	4869	4428
S06	−15.4	−123.4	−13.5	−97	4518	4062
S07	−16.5	−130.6	−14.6	−105	4999	4576
S08	−20.1	−157.6	−15.5	−111	6174	5791
S09	−15.9	−126.6	−15.1	−108	4883	4379
S10	−20.7	−148.0	−14.8	−106	5719	5969
S13	−20.8	−156.0	−14.7	−105	6075	6018
S14	−20.3	−154.8	−14.7	−105	6019	5842
S15	−20.4	−157.3	−14.1	−100	6094	5842
S16	−19.7	−152.6	−13.9	−99	5861	5594
S17	−20.2	−153.7	−14.0	−100	5893	5757
S18	−20.6	−156.4	−13.5	−96	6018	5908
S19	−20.7	−155.8	−13.8	−98	6003	5934

5.2. Origin of Ions

5.2.1. Major Ion

The types of spring water samples in the LFZ are mainly HCO_3^--Na^+, and a small number of samples are HCO_3^--Na^+·Ca^{2+} and HCO_3^-·Cl^--Na^+ types according to Shchukarev classification [44]. Based on the analysis of the major ions of the spring water samples, a Piper diagram (see Figure 4) was drawn to further illustrate the groundwater hydrochemical types in the Litang fault zone [45]. A HCO_3^--Na^+ type hot spring is mainly caused by deep circulation of large faults. A HCO_3^--Na^+·Ca^{2+} type hot spring is often formed by the mixing of HCO_3^--Na^+ type hot spring water and shallow cold water. A HCO_3^-·Cl^--Na^+ type hot spring is formed in geothermal system with high-temperature fracture and deep circulation. The main cations in the LFZ are Na^+ and Ca^{2+}, and the Mg^{2+} is less common [46]. The hot spring water collected from LFZ has relatively low ionic salinity, ranging from 7.0 to 83.7 meq/kg, as illustrated in the correlation plot of Na^++K^+ vs. Ca^{2+}+Mg^{2+} (see Figure 5). The S14, S02, and S04 samples have low ionic salinity, indicating that the ascending of those spring water is faster and is not or weakly mixing with Ca^{2+}- and Mg^{2+}-rich cold waters. On the contrary, hot springs with higher Ca and Mg contents are due to mixing with cold water and/or re-equilibration upon infiltration of thermal water in shallow aquifers hosted in alluvial and fluvial deposits [47,48]. The main anion is HCO_3^-, followed by Cl^- and SO_4^{2-}, which in is agreement with results of Zhao et al. [46]. The ion concentration of Na^+ is linked with the runoff time of underground hot water. The high concentration of Na^+ indicates that the runoff of underground hot water is long and the thermal circulation is deep [49]. The lithology of the fault zone is mainly metamorphic rock and granite. Due to dissolution and filtration in the water–rock process, various feldspar, e.g., albite, in the rock react with the geothermal water, resulting in the relatively large concentration of Na^+ and HCO_3^- in the geothermal water [46].

The cation exchange is an important process that controls hydrochemical features. Both CAI 1 and CAI 2 are negative values, indicating that reverse cation exchange has occurred in water samples collected from LFZ (see Figure 6). Ca^{2+} and Mg^{2+} produced by carbonate rock dissolution in groundwater exchange with Na^+ and K^+ in the surrounding rock of the tunnel. The adsorption of Ca^{2+} and the release of Na^+ explain the increase in Na^+ in water samples, which will also lead to the change of chemical composition of water [50]. The concentration of HCO_3^- in hot spring water in the LFZ is high, which may be related to strong water–rock interaction with limestone strata of the hydrothermal system [7]. Besides the medium-deep materials, the mafic volcanic breccia, basalt, mafic tuff intercalated slate, limestone, and siliceous rock strata of Mesozoic Triassic Qugasi

Formation, which are involved due to fault activities, may be one of the sources of Maoya hot spring materials [51].

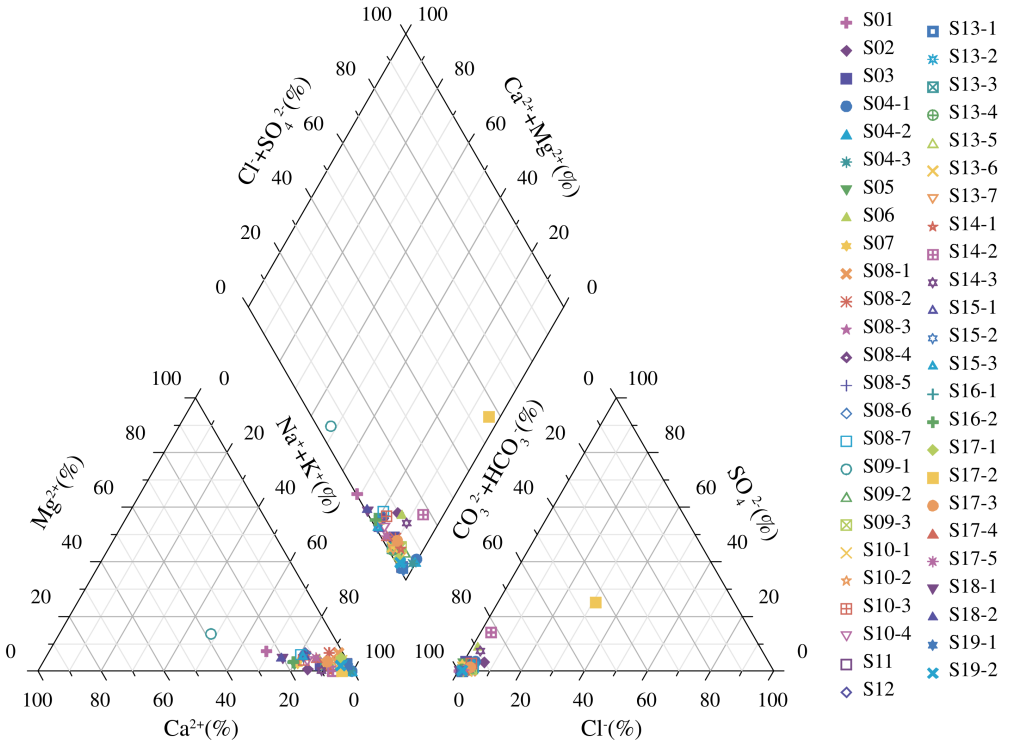

Figure 4. Piper diagram of hot spring waters in the LFZ.

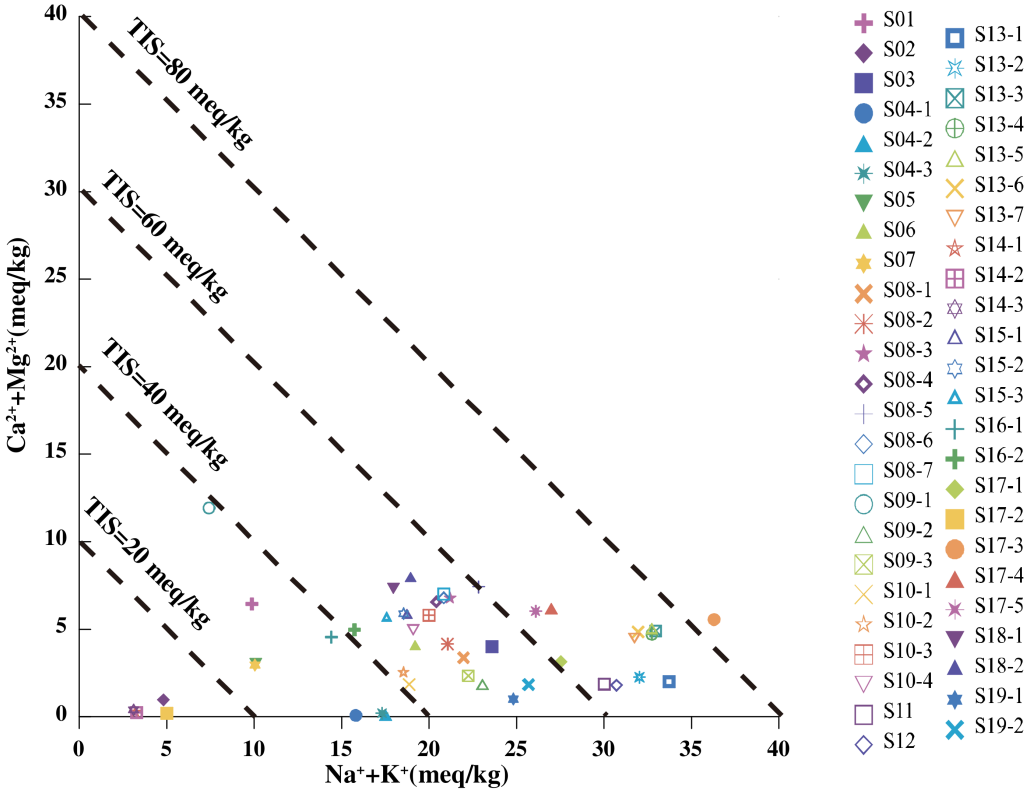

Figure 5. Correlation plot of $Na^+ + K^+$ vs. $Ca^{2+} + Mg^{2+}$ for the spring water samples collected from LFZ, also showing iso-ionic-salinity (TIS) lines for reference.

Cluster analysis is carried out by Gaussian Mixture Model with Origin 2021b software (see Figure 7). Chlorine, $\delta^{18}O$, and $\delta^{2}H$ are used as data sources for cluster analysis, respectively. The results show that hot spring water in the LFZ comes from three sources. It can be concluded that the hot springs to the north of LFZ belong to Group 1, and the other type is represented by S08 and S09 hot springs, belonging to Group 2, and the hot springs on Litang fault belong to Group 3. Among them, the hot spring of Group 2 has a mixed effect with the other two groups of hot spring groundwater. The results of three-dimensional clustering show this feature more clearly. Three-dimensional clustering is closer to the results of Cl and $\delta^{18}O$ clustering analysis, and is consistent with the spatial distribution of hot springs in the LFZ.

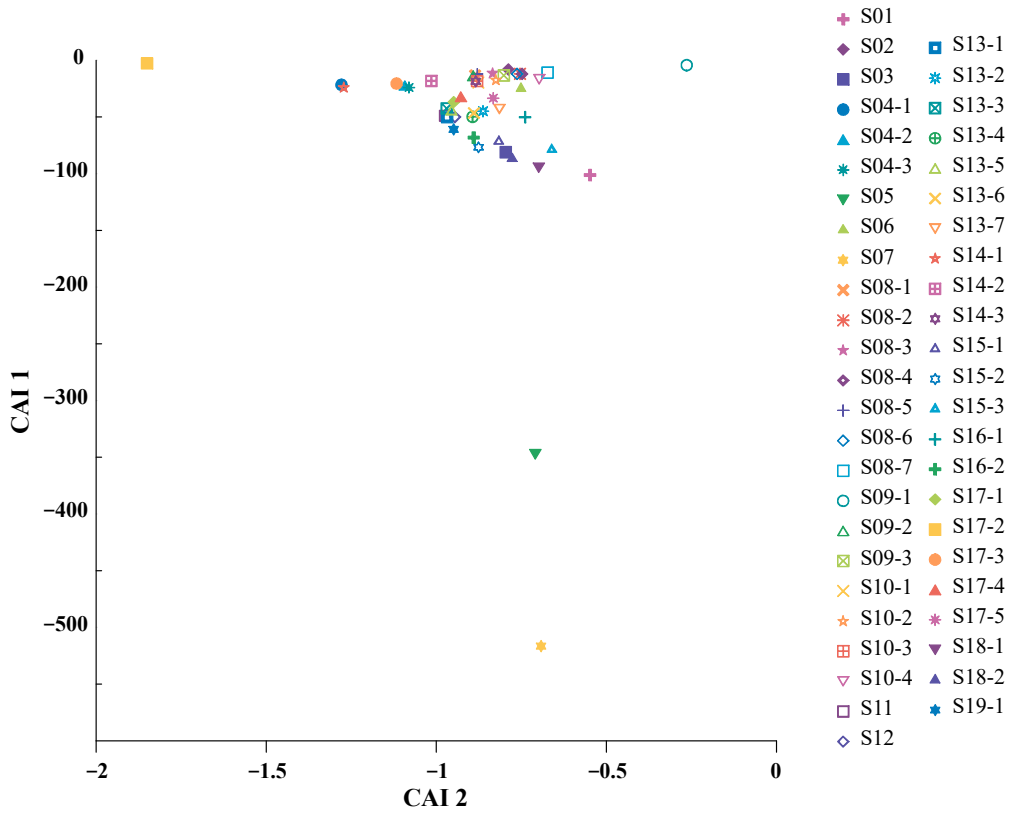

Figure 6. Scatter plot of CAI 1 against CAI 2.

Saturation Index (SI) indicates whether a solution is in equilibrium with the solid phase, or whether it is undersaturated or oversaturated in terms of a specific mineral or various minerals. Generally, presuming that when the SI is in the range of −0.2 to 0.2, the corresponding mineral is in equilibrium. Positive SI values correspond to oversaturation (precipitation), while negative values correspond to undersaturation (dissolution) of a specific mineral [52]. The sulfate minerals are undersaturation, such as anhydrite and gypsum, indicating that minerals are usually dissolved. Some of LFZ hot spring water samples contain carbonate minerals, such as aragonite, calcite and dolomite. Except for the aragonite and calcite of S06 hot spring water, carbonate minerals of other samples are undersaturated.

The samples collected from the hot springs in the Litang fault were simulated and the saturation indices of aragonite, calcite, and dolomite minerals were not calculated, which may be linked to their deposition. In terms of SiO_2 minerals, chalcedony and quartz are in equilibrium or close to an equilibrium state, in which chalcedony is dominated by dissolution, while quartz is dominated by precipitation. The silicate minerals containing Mg, such as chrysotile, sepiolite, and talc, show the state of undersaturation or oversaturation, and the difference between samples is relatively large. F-containing minerals, such as

fluorite, are in equilibrium in some samples, and in undersaturation state in other samples due to dissolution. The halite in all samples is undersaturated. Overall, the mineral composition of LFZ hydrochemical samples is less in equilibrium, most minerals are in undersaturated state, and the negative values of SI are relatively larger, only a few minerals are in oversaturated state (see Figure 8).

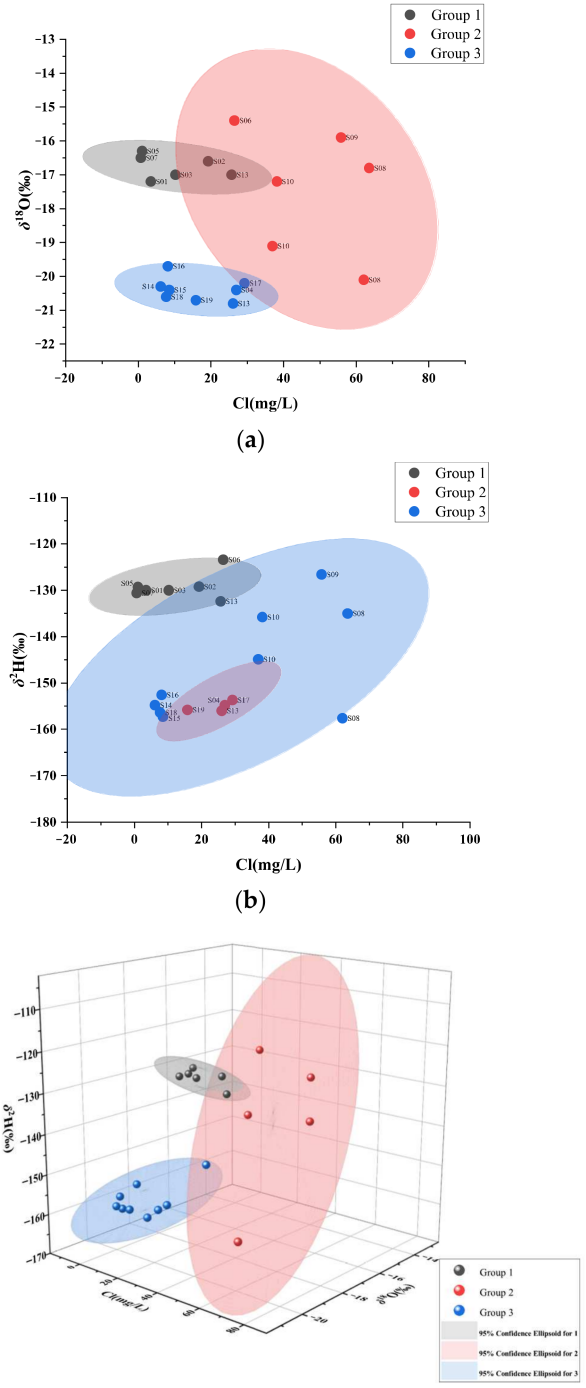

Figure 7. The plot of $\delta^{18}O$ relative to chloride (**a**), $\delta^{2}H$ relative to chloride (**b**), and the clustering result (**c**) for the hot spring water samples from the LFZ.

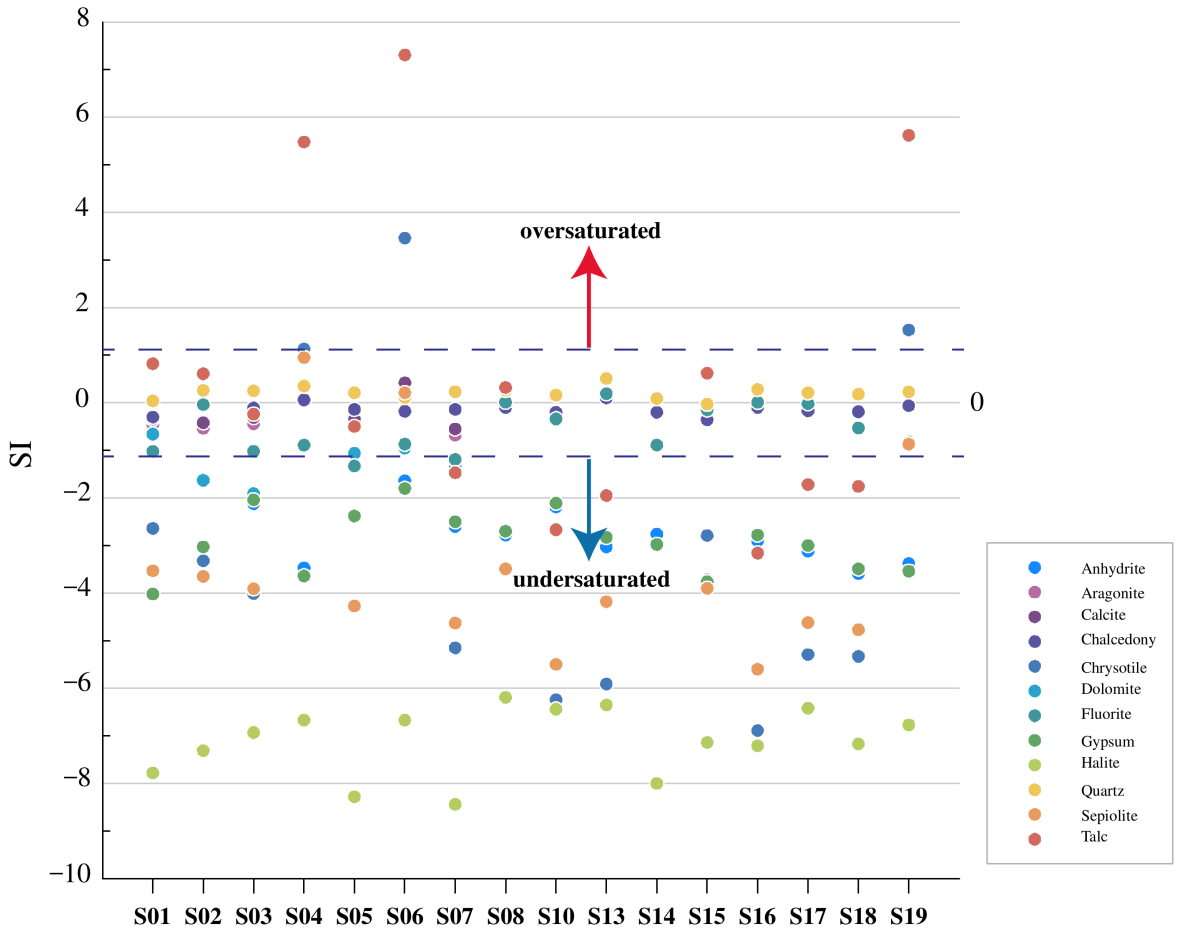

Figure 8. Saturation indices at outlet temperature of the hot spring water samples in the LFZ.

According to the simulation results of dissolved minerals in hot spring water based on PHREEQC database, the number of dissolved minerals of the LFZ hot spring waters obtained by simulation can be divided into three categories: 12 mineral types, 9 minerals, and 7 minerals. Except S04 hot spring located on the Litang fault, other hot springs (S01~S03 and S05~S07) located in the northern part of the study area and not on the fault are all simulated to obtain 12 kinds of minerals. Except S14 spring located at the intersection of the middle and southern segment of Litang fault, other hot springs located in the southern part of the study area and on the fault are all simulated to obtain nine minerals. Among LFZ hot springs, S14 hot spring has the least types of dissolved minerals, only seven minerals. S04 and S14 hot springs have regional particularity in the number of mineral species, which may indicate that the underground flow process distinct from other hot springs or other hot springs on the basis of mixing with shallow groundwater and water–rock reaction.

In Figure 9, the saturation indices calculated for completely ordered and completely disordered dolomite are plotted against the calcite saturation index. The hot springs on the Litang fault zone have no calcite and dolomite (see Supplementary Table S4). The hot springs to the north of the Litang fault zone have these two minerals. The solutions are in equilibrium with calcite; except for the S06 hot spring, the solutions are also in equilibrium with ordered dolomite, but the disordered dolomite are undersaturated. For the S06 hot spring water sample, the ordered dolomite in the state of oversaturation, stable phase in the low-temperature environment, could be linked to both nonstoichiometric dolomite presence (with Ca^{2+} excess), and higher cation disorder and consequent kinetic reasons [53,54].

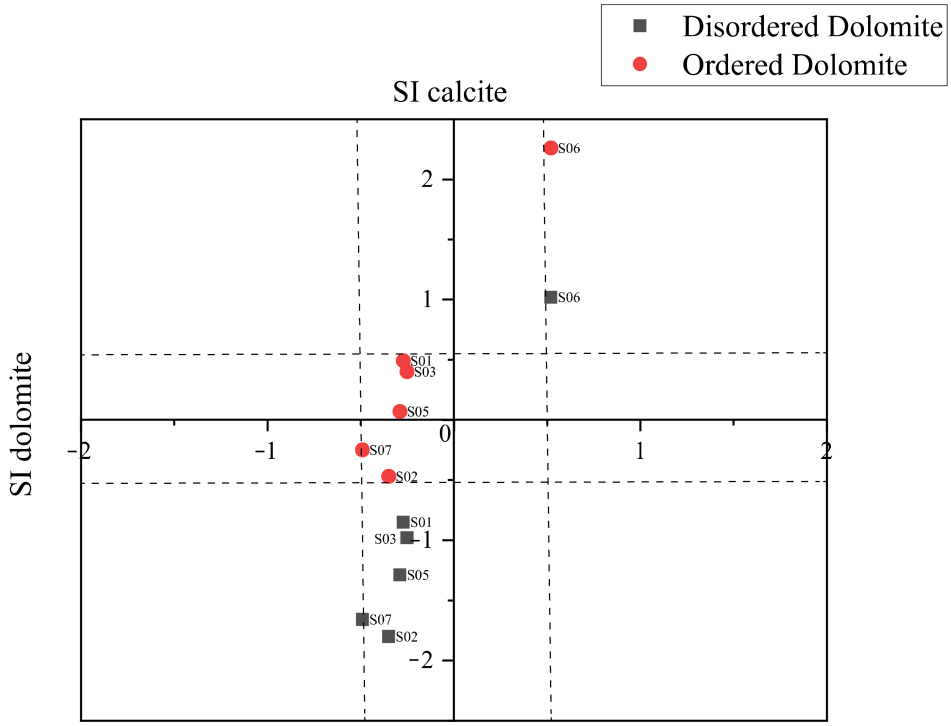

Figure 9. Saturation index of calcite vs. saturation indices of ordered/disordered dolomite.

5.2.2. Trace Elements

The Cl/B ratio tends to indicate a common reservoir source for hot spring water. Lithium termed the "rare alkali", is deemed as part of the soluble or conservative species, and is used with Cl to characterize water from common sources [8,55]. As is shown in Figure 10, Cl versus B and Cl versus Li for hot spring water in the LFZ are plotted. Two straight lines and a cluster of points can be recognized by fitting the points in the Cl versus B plot.

In the plot of Cl vs. B, the S19, S13, and S09 springs can be fitted as straight line, and S04 and S10 spring can be fitted as another line; however, the symbols of S08 hot spring constitute a relatively independent cluster in the plot of Cl vs. B and Cl vs. Li., and the Cl vs. B and Cl vs. Li have no linear relationship with other hot springs, indicating that S08 hot spring may have a relatively independent source. This phenomenon indicates that the hot springs in the LFZ may derive from at least two discrete heat sources, but it is more likely to be from three heat sources. The direction of groundwater flow can be approximately determined by the increase in B/Li ratio along the flow direction [55]. The B/Li ratios of S09 and S15 hot springs are 4.51~7.64, S11~S13 hot springs are 6.50~7.04, S16 hot spring is 7.07~8.54, S18 and S19 hot springs are 8.11~9.86, and the S14 hot spring is 13.33~15.12. It shows that groundwater flows roughly from north to south. It is worth noting that although S15 and S14 hot springs are concentrated in spatial location, the source of S14 hot spring may be shallower than other hot springs, and groundwater may flow a long distance before reaching S14 hot spring. The B/Li ratio of S04 hot spring is 2.26~2.55, which is the lowest ratio in the region. The B/Li ratio of S17 hot spring is 5.62~8.67, which changed greatly in 2016 (8.67) compared with the samples collected in 2010 (5.90), 2017 (6.41), and 2018 (5.62). The B/Li ratio of S10 hot spring is 6.89~7.19. The groundwater flows roughly from north to south, when the flow reaches the position of S17 spring, and turns north. The B/Li ratio of S08 hot spring is 13.93~20.75, and the concentration of Cl^- is high, which may be from an independent reservoir source.

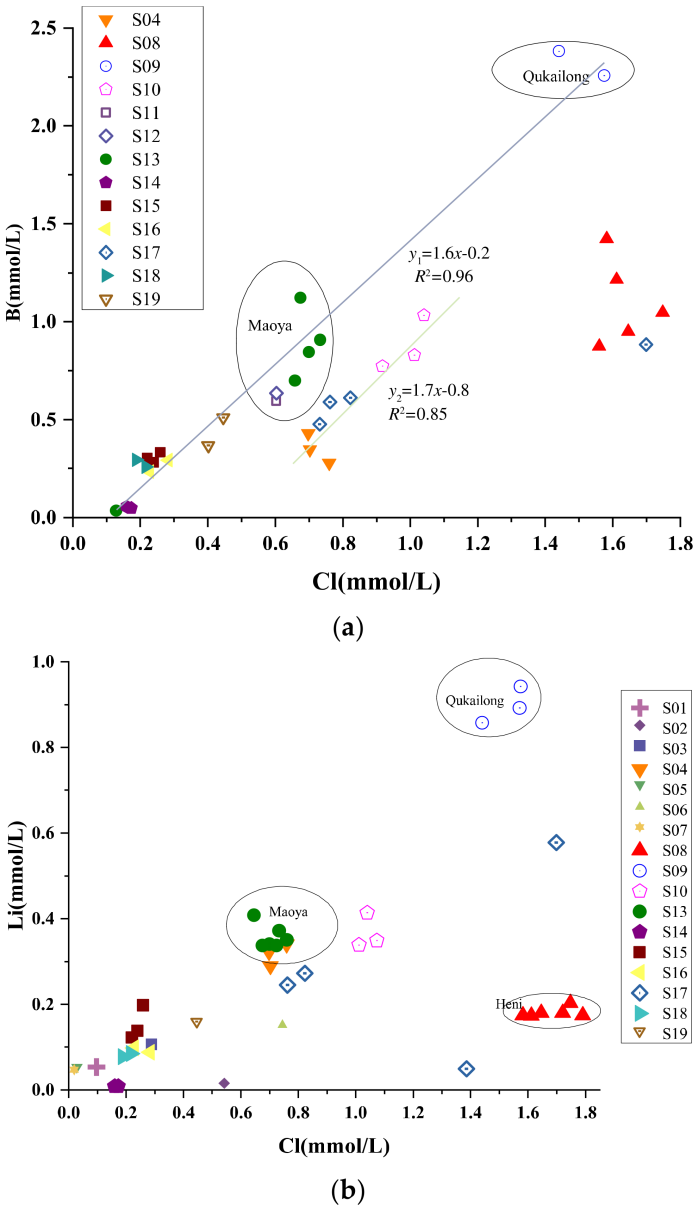

Figure 10. Plot of Cl versus B (**a**) and Cl versus Li (**b**) for hot spring water in LFZ.

A total of 45.8% of the variance can be explained by Principal Component Analysis (PCA, performed by Canoco 5 software) in the data by the first two ordination axes (see Figure 11) [56]. The first axis is primarily explaining gradients in Ca^{2+}, Mg^{2+}, Ba^{2+}, and Sr^{2+} concentrations; HCO_3^- concentration (negative); and pH, temperature, and Al^{3+} and F^- concentrations (positive), whereas the second axis explains primarily gradients in Cl^-, B, and Cu. From the perspective of major and trace elements, the springs on the LFZ can be divided into high-chlorine springs, medium-chlorine springs, low-chlorine springs, and high-aluminum springs. High-chlorine springs include S09, S13, S17, and S08 hot springs; middle-chlorine springs include S10, S11, S12, S15, S16, and S19; low-chlorine springs are S18 and S14; and the high-aluminum spring is S04. The high-chlorine spring is rich in Cl and B components, which may have more deep information and should be the focus of seismic monitoring in the LFZ.

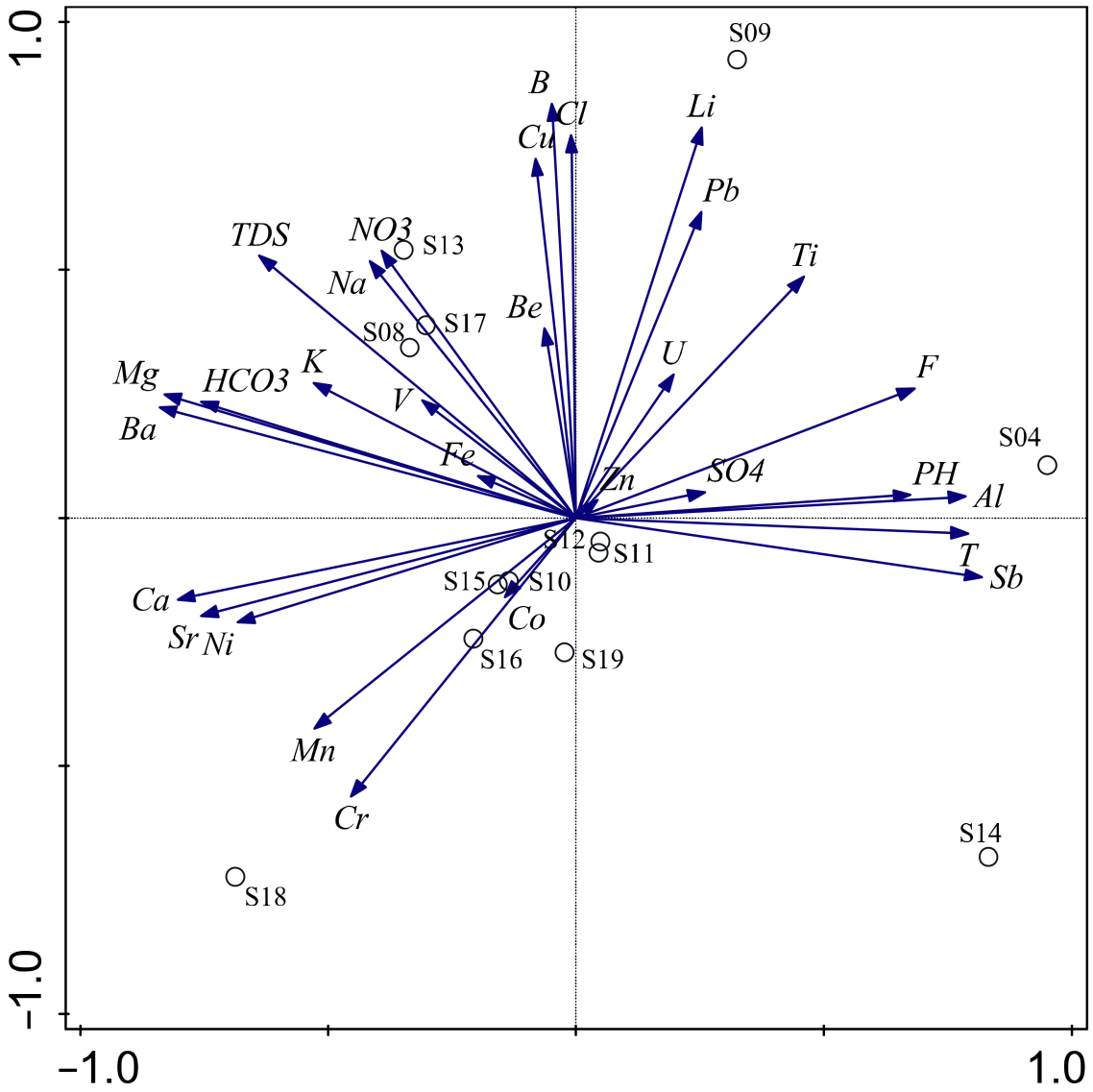

Figure 11. PCA ordination diagram of geochemical parameters (arrows) and sampling locations (points).

The element contents in a hot spring depend on the water–rock reaction during deep circulation of groundwater; therefore, trace elements in hot springs can reflect the degree of water–rock reactions to some extent [57]. The trace element composition of Qugasi sandstone rock is used as the reference value. Ni is chosen as the reference element [58]. The normalized result is shown in Figure 12, and the trace elements involved in the investigation include Sc, V, Cr, Co, Rb, Sr, Y, Nb, Cs, Ba, La, Ce, Pr, Nd, Sm, Eu, Gd, Tb, Dy, Ho, Er, Tm, Yb, Lu, Pb, Th, and U (see Supplementary Table S5). Compared with other hot springs, EF_{Ni} of most trace elements from S04 hot spring are closer to 1. It can be noted that the trace elements in Qugasi formation and those of S04 springs with the shortest groundwater flow have strong consistency, indicating that the source of trace elements of S04 hot spring are strongly related to rock dissolution. In spring water of LFZ, Sc, Cr, Rb, Sr, Cs, Ba, and Eu elements are enriched, and the degree of Cs element enrichment is the highest (see Figure 12).

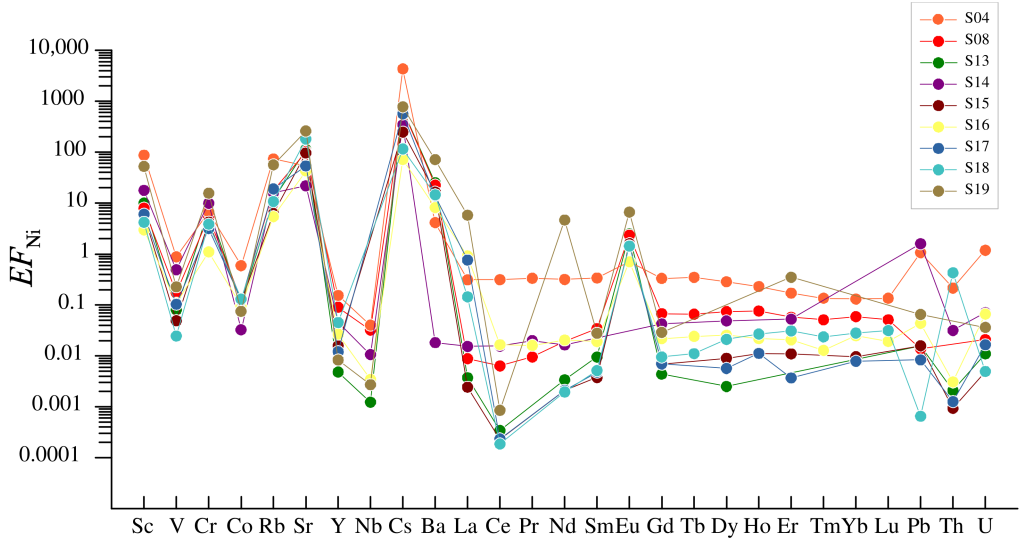

Figure 12. Enrichment coefficients for spring water collected in the LFZ normalized by Ni element.

The radiogenic strontium isotope ($^{87}Sr/^{86}Sr$) ratio is robust for provenance identification [59]. If Rb and Sr are incorporated into a mineral or rock during its formation and the system remains closed with respect to these elements, then the amount of ^{87}Sr increases with time as the radioactive ^{87}Rb decay. The amounts of ^{84}Sr, ^{86}Sr, and ^{88}Sr remain constant. Therefore, older rocks generally have a higher $^{87}Sr/^{86}Sr$ ratio than younger rocks with the same initial Rb/Sr ratio. Over geological time, rocks with a given age composed of minerals with a high Rb/Sr will develop a higher $^{87}Sr/^{86}Sr$ ratio than rocks with a lower Rb/Sr. Thus, the $^{87}Sr/^{86}Sr$ ratio of geological materials can be employed as a proxy of both age and geochemical origin [60]. $^{87}Sr/^{86}Sr$ ratio of volcanic, plutonic, and metamorphic basic rocks, plutonic and metamorphic acid rocks, limestone, sandstone, and shales are 0.7028~0.7071, 0.7038~0.7057, 0.7107~0.8644, 0.7062~0.7156, 0.7074~0.7536, and 0.7279~0.7547, respectively [61]. The $^{87}Sr/^{86}Sr$ ratios of carbonates are 0.705~0.710, and most of the ratios are around 0.708 [61,62]. The relationship between $^{87}Sr/^{86}Sr$ and Sr concentration of hot springs is plotted in Figure 13. Additionally, the range of $^{87}Sr/^{86}Sr$ ratios of the above-mentioned rocks is marked. The $^{87}Sr/^{86}Sr$ ratios of S04, S08, S10, S13, S14, S15, S16, S17, S18, and S19 hot springs are relatively high, and their Sr isotopic compositions may come from sandstone or plutonic and metamorphic acid rocks (see Supplementary Table S6). The strontium composition of the S13 and S16 hot spring water may also derive from limestone and shale, respectively.

As mentioned in Section 5.2.1, the main hydrochemical type of LFZ hot springs is HCO_3^--Na^+. The HCO_3^--Na^+ type geothermal water is formed by chemical reactions among infiltrated meteoric water, dissolved carbon dioxide, and reservoir rocks containing albite and microcline as major minerals [63,64]. The relatively higher $^{87}Sr/^{86}Sr$ ratios of hot spring water reflect that groundwater interactions with marine carbonates and/or silicate minerals with slightly higher $^{87}Sr/^{86}Sr$ ratios than the carbonates. Therefore, the $^{87}Sr/^{86}Sr$ ratios of hot spring water in the LFZ illustrate that the weathering of old silicate minerals with high $^{87}Sr/^{86}Sr$ ratio in the sedimentary environment is an important source of major ions, especially Na^+ and HCO_3^- and dissolved silica in the geothermal water [65]. The lithology of the Upper Triassic Qugasi formation is complex, including crystalline limestone, bioclastic limestone, metamorphic sandstone and slate intercalated metamorphic mafic-intermediate volcanic rocks [66]. The ratios of radiogenic strontium in the southeastern Qinghai–Tibet Plateau are highly variable and more radiogenic, ranging from 0.70553~0.73019. The extremely complex lithology of the southeastern margin of the Qinghai–Tibet Plateau, where a large amount of Paleozoic–Mesozoic sedimentary rocks, low–high metamorphic rocks, and granitoids are involved, may lead to the highly heterogeneous Sr isotope range in this region [67].

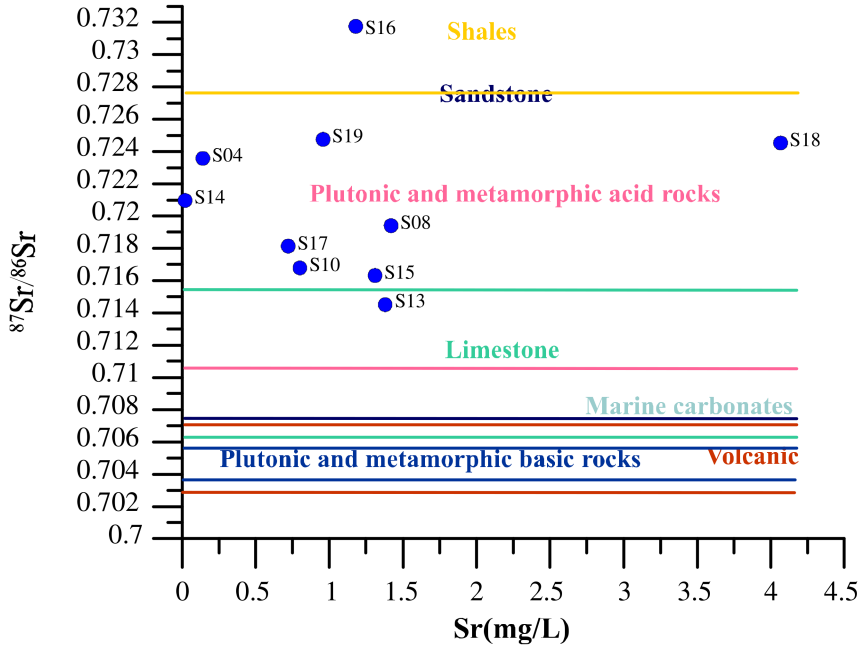

Figure 13. The plot of Sr concentration versus $^{87}Sr/^{86}Sr$ ratio of hot springs in the LFZ.

5.3. Water–Rock Reactions

5.3.1. Determination of Equilibrium Condition

The Na-K-Mg ternary diagram proposed by Giggenbach [68] is typically used for the determination of water–rock equilibrium conditions. The hot spring water in volcanic hydrothermal systems, active tectonic areas, continental geothermal areas can be evaluated with Na-K-Mg ternary diagram, which divides spring water into fully equilibrated, partially equilibrated and immature water [69]. As is shown in Figure 14, hot spring water in the Litang fault zone is mostly immature water. However, the S04 hot spring water is partial equilibrium, which is located on the isothermal line of 220~240 °C, and may be related to near Yidun area [7]. The water samples collected from the S14 hot spring are located in the equilibrium water region, on the isothermal line of 160~180 °C. The hydrochemical composition of S17 hot spring collected in 2015 is quite different from that of samples collected in other years, which is located on the isothermal line of 180~200 °C. The flow distance of thermal water from S04 hot spring is relatively short, is partial equilibration, whose hydrochemical composition is greatly affected by metamorphic sandstone. Except for the S14 hot spring, other hot springs are immature water, which may be recharged by precipitation or mixed with cold shallow groundwater, or more or less affected by carbonate rocks in flowing region.

Consistent with the results of Hou et al. [7], it can be found from the 10 K/(10 K + Na) versus 10 Mg/(10 Mg + Ca) binary diagram that most of the hot springs in the LFZ deviate from the full equilibrium line, with high Ca and Mg concentration, reflecting the rapid equilibrium of K-Mg and mixing with shallow Ca-Mg-rich water [70]. The 10 K/(10 K + Na) values of S04 hot springs in Figure 15 are in the range of 0.3~0.4, which can be roughly inferred that the reservoir temperature is about 180 °C. S14 and S02 hot springs, S16 and S18 hot springs may belong to two groups of different reservoir temperatures. The reservoir temperature of the former group is about 120~140 °C, and that of the latter group is about 220~240 °C, which indicates that LFZ hot spring water may come from different thermal reservoirs. The majority of hot springs in the LFZ are located in a nonequilibrium state and may be affected by mixing (dilution) processes [7].

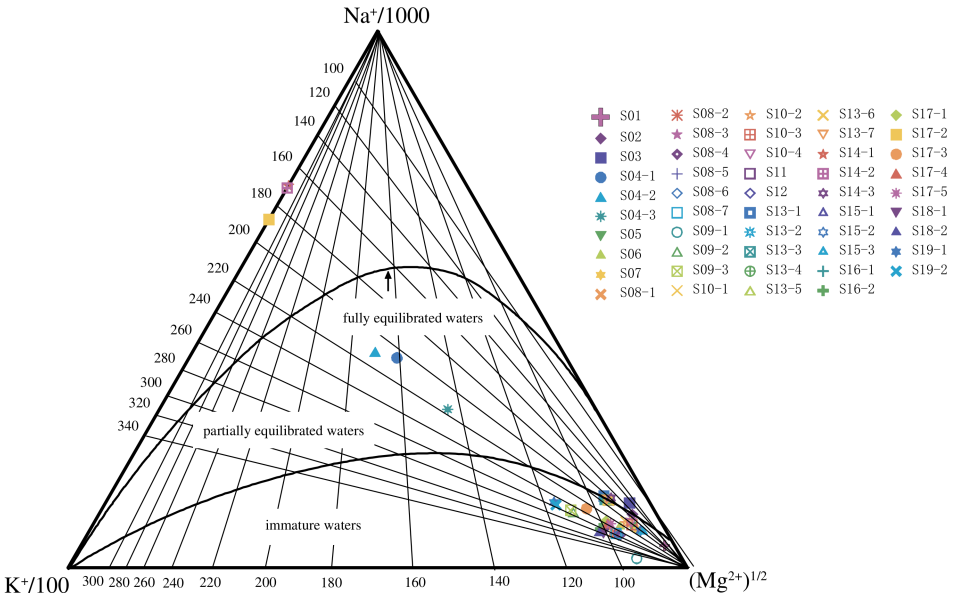

Figure 14. Na-K-Mg ternary diagram of hot spring water in the LFZ.

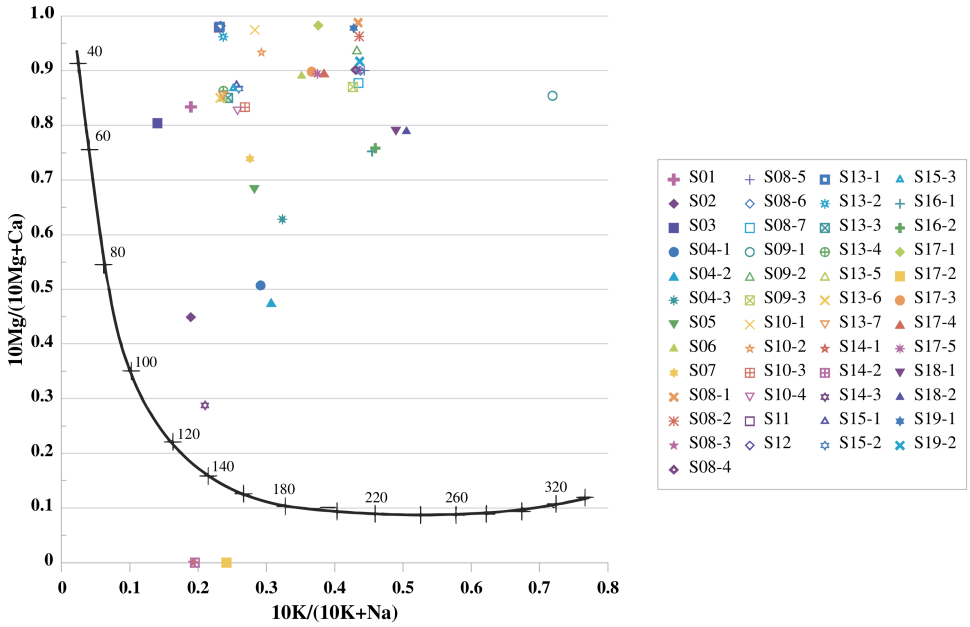

Figure 15. The 10 Mg/(10 Mg + Ca) versus 10 K/(10 K + Na) binary diagram.

5.3.2. Reservoir Temperature and Circulation Depth

Solute geothermometers are widely used as valuable tools to estimate the reservoir temperature of the geothermal field. The assumption is the case that the concentration of elements or species acting as geothermometer is controlled only by a temperature-dependent mineral–fluid reaction. The reaction attains equilibrium in the reservoir, and after the fluid exits the reservoir, it flows rapidly to the surface with no re-equilibration, mix or diluting process [55]. However, this assumption is very harsh, which is hard to obtain in many cases in the natural environment. In fact, it is relatively slow to arrive at the equilibrium state in the reservoir. The dilution or mixing process still may occur during the ascent of thermal fluid to the earth's surface [71]. Therefore, reservoir temperatures calculated by different geothermometers are also different.

The quartz geothermometer is appropriate for relatively low temperature reservoir (<250 °C), too high-temperature will lead to the deposition of silica during ascent of geothermal water [72]. Reservoir temperatures calculated by silica–quartz/chalcedony-based geothermometers are significantly lower than that calculated by ion concentration. The re-equilibrium rate of Na-K exchange is slower than that of SiO_2 dissolution-precipitation. The advantage of the Na/K geothermometer is that when thermal water rises to the surface, the equilibrium condition at the depth is preserved for a long time. Therefore, the Na/K geothermometer can indicate higher temperatures at a deeper level [55,68]. The Na/Li geothermometer seems to be effectively applied to low- to high temperature geothermal systems [73]. Except for S04 hot spring, the reservoir temperatures of other springs obtained by Li-Mg geothermometer are relatively low, which are close to that obtained by quartz geothermal thermometers [74]. Na-K-Ca geothermometer is suitable for the case of additional Ca dissolve in the process of geothermal water ascending, which is easily affected by dilution and carbonate equilibrium in the system. The high content of magnesium in geothermal water will also affect its application effect [75,76]. Ca/Mg geothermometer is suitable for hot spring water coming from the medium-low temperature hydrothermal systems which are hosted in carbonate-evaporite rocks [77].

The reservoir temperatures estimated by chalcedony, quartz, Na-K-Ca, Na/Li, Na/K, Li-Mg, Na-K-Ca, and Ca/Mg geothermometers are listed in Table 2.

Table 2. Reservoir temperatures (°C) estimated using different geothermometers for hot springs in the LFZ.

Sample ID	Chalcedony No Steam Loss	Chalcedony Steam Loss	Quartz No Steam Loss	Quartz Steam Loss	Na/K	Na/Li	Li-Mg	Na-K-Ca	Ca/Mg
S01	27.3	34.1	59.5	65.5	168	174	59.8	140.9	36.7
S02	50.9	54.3	82.1	85.4	168	121	57	140.9	153.0
S03	38.8	44.1	70.6	75.3	147.3	160.5	81.4	125.5	46.3
S04-2	91.5	88.0	119.9	118.1	210.7	258.3	210.7	172.2	143.6
S05	40.2	45.2	71.9	76.4	202.1	160.7	69.9	165.8	81.8
S06	55.2	57.9	86.1	88.9	225.8	194.5	85.3	182.9	15.7
S07	33.3	39.3	65.3	70.6	199.9	159.1	66.9	164.3	65.8
S08-5	38.8	44.1	70.6	75.3	257.8	206.4	85.5	205.1	11.5
S10-3	29	35.6	61.1	66.9	197.3	262.7	113.1	162.5	36.9
S13-5	38.8	44.1	70.6	75.3	185.9	219.1	110.8	154.2	30.7
S14-2	61.1	62.9	91.7	93.8	170.3	138.1	—	142.6	—
S15-2	27.3	34.1	59.5	65.5	194.2	193	81.1	160.3	24.9
S16-2	33.8	39.8	65.8	71.1	263.5	185.2	80.8	208.9	60.2
S17-4	26.5	33.4	58.7	64.7	237.1	213.4	95.9	190.8	13.5
S18-2	27.5	34.3	59.7	65.7	280.4	168	70.3	220.3	51.0
S19-2	67.1	67.9	97.4	98.7	255.3	184.3	95.9	203.5	4.0

The estimated reservoir temperatures of Na/K, Na/Li, and Na-K-Ca geothermometers are generally higher than those of silica-quartz/chalcedony-based, Li-Mg and Ca/Mg geothermometers. Affected by SiO_2 re-equilibration and mixing with Ca-Mg-rich shallow water, the silica and Li-Mg geothermometers are much lower than the other cation geothermometers, which may be sometimes difficult to the actual reservoir temperatures. Thus, the Na/K, Na/Li, and Na-K-Ca geothermometers tend to provide more reliable reservoir temperatures. However, the application of Na/K thermometer needs the albite and potassium feldspar reach equilibrium state in the reservoir. Obviously, hot springs in the LFZ hot spring do not meet the criteria, and the reservoir temperatures estimated by Na/K geothermometer can only be considered as a reference. Ca/Mg geothermometer is suitable for low-temperature reservoir in carbonate rocks, but the calculated reservoir temperature is too low, even lower than the temperature of hot spring water; therefore, it is considered not suitable for hot springs in the LFZ. The Na/Li of the deep fluid is thought to be preserved on ascent to the surface. Considering that there may be carbonate thermal reservoirs, the Ca/Mg system is affected by Ca-mineral precipitation. The Na/Li geothermeter seems to be the most reliable to evaluate the deep temperatures inside the confined parts of the carbonate reservoir [78]. Therefore, the Na/Li thermometer is used to estimate reservoir temperatures and circulation depths. The reservoir temperatures of S01, S02, and S03 hot springs a little farther from the Litang fault are lower. The reservoir

temperature of S04 hot spring obtained by all geothermometers is relatively high, indicating that it has a high reservoir temperature.

The spatial locations and reservoir temperatures of S03, S05, S06, and S07 hot springs are alike, and the hydrothermal fluid is likely to originate from the same reservoir. S10, S15, S16, S18, and S19 hot spring water originate from the same reservoir, and compared with them, the reservoir temperature of S08 hot spring is higher, and that of S14 hot spring is lower. S15, S16, S18, S17, and S19 hot springs have roughly similar hot reservoir temperatures, which may come from the same reservoir. It can be seen from the difference of reservoir temperatures calculated by geothermometers that there should have different heat sources. Positive correlation exists between circulation depth of geothermal water and its temperature, and the circulation depth (H) can be roughly calculated by

$$H = \frac{T_1 - T_2}{I} + h \quad (8)$$

where T_1 is the reservoir temperature (°C), T_2 is the local annual average temperature (°C), I is the geothermal gradient (°C/100 m), and h is the thickness of constant temperature zone [79]. The annual average temperature in western Sichuan is 3.0 °C, the geothermal gradient is ~4.75 °C/100 m, and the thickness of the constant temperature zone is 20 m [49,79]. The reservoir temperature can be obtained by Na/Li geothermometer, e.g., the reservoir temperature for S01 spring estimated by Na/Li geothermometer is 174 °C, and the corresponding circulation depth can be calculated by Equation (8) based on reservoir temperature, is 3620 m. As is shown in Table 3, the circulation depths of springs in the LFZ calculated based on Na/Li geothermometer is 2504~5487 m.

Table 3. Circulation depths estimated by reservoir temperatures for hot springs in the LFZ.

Sample ID	Reservoir Temperature (°C)	Air Temperature (°C)	Circulation Depth (m)
S01	174.0	3.0	3620
S02	121.0	3.0	2504
S03	160.5	3.0	3336
S04-2	258.3	3.0	5395
S05	160.7	3.0	3340
S06	194.5	3.0	4052
S07	159.1	3.0	3306
S08-5	206.4	3.0	4302
S10-3	262.7	3.0	5487
S13-5	219.1	3.0	4569
S14-2	138.1	3.0	2864
S15-2	193.0	3.0	4020
S16-2	185.2	3.0	3856
S17-4	213.4	3.0	4449
S18-2	168.0	3.0	3494
S19-2	184.3	3.0	3837

5.3.3. Cold Water Mixing Ratio

The hot spring water samples collected from LFZ are located in immature water and partially equilibrated water zone, which may have cold water mixing. By calculating the SI of unlike mineral compositions at different temperatures, the equilibrium state of hydrothermal minerals can be evaluated and the reservoir temperature can be estimated [80]. After underground thermal water reaches equilibrium in the reservoir, as geothermal water rises to the surface, the disequilibrium conditions may exist due to the mixing, dilution, ebullition and phase separation of water [52]. As is shown in Figure 16, the equilibrium temperature is identified in S04 hot spring around 110 °C. The equilibrium temperatures in S16, S08, and S13 hot springs are around 75 °C, 75 °C and 70 °C, respectively. The equilibrium temperature in S14 hot spring is 110 °C, and in S19 hot spring is 100 °C. The reservoir

temperatures obtained by quartz mineral equilibrium method are basically consistent with that obtained by quartz geothermometer.

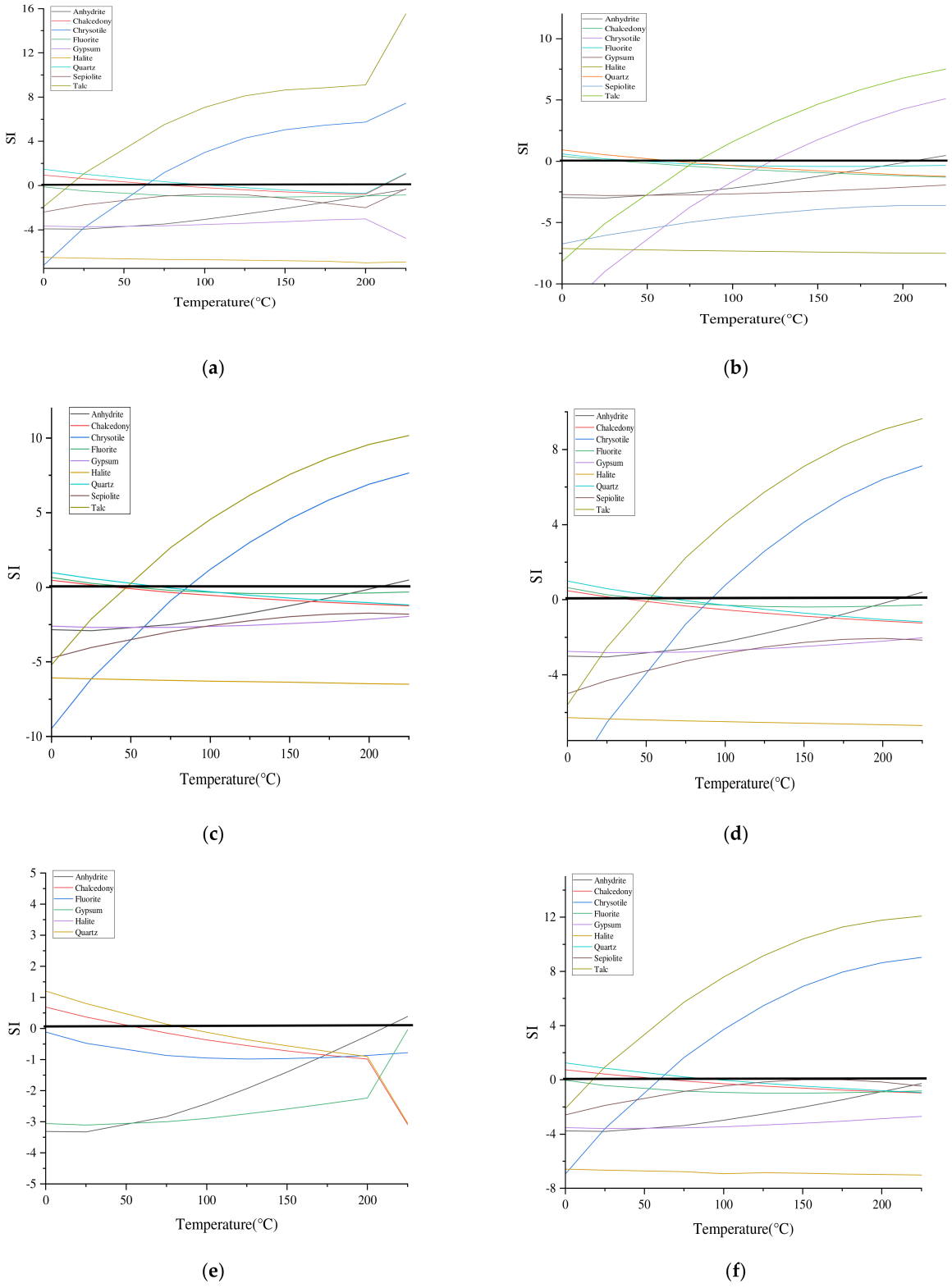

Figure 16. Saturation indices vs. temperature for the hot spring water samples in the LFZ. (**a**) S04. (**b**) S16. (**c**) S08. (**d**) S13. (**e**) S14. (**f**) S19.

The silicon-enthalpy model is utilized to eliminate the influence of cold-water mixing, and the proportions of cold-water mixing and the thermal reservoir temperatures before mixing are analyzed [79]. Previous study has shown that the temperature of Litanghe River water sample is 12.7 °C, and the concentration of SiO_2 is less than 0.1 mg/L, in order to facilitate the calculation of SiO_2 concentration is 0.1 mg/L [81]. Silicon-enthalpy models of S04, S16, S08, S13, S14, and S19 hot springs are established, as is shown in Figure 17. Thermal reservoir temperatures of S04, S16, S08, S13, S14, and S19 hot springs are 175 °C, 125 °C, 125 °C, 200 °C, 113 °C, and 131 °C, respectively. The mixing ratios of cold water to S04, S16, S08, S13, S14 and S19 hot springs are 0.62, 0.73, 0.66, 0.89, 0.32, and 0.50, respectively.

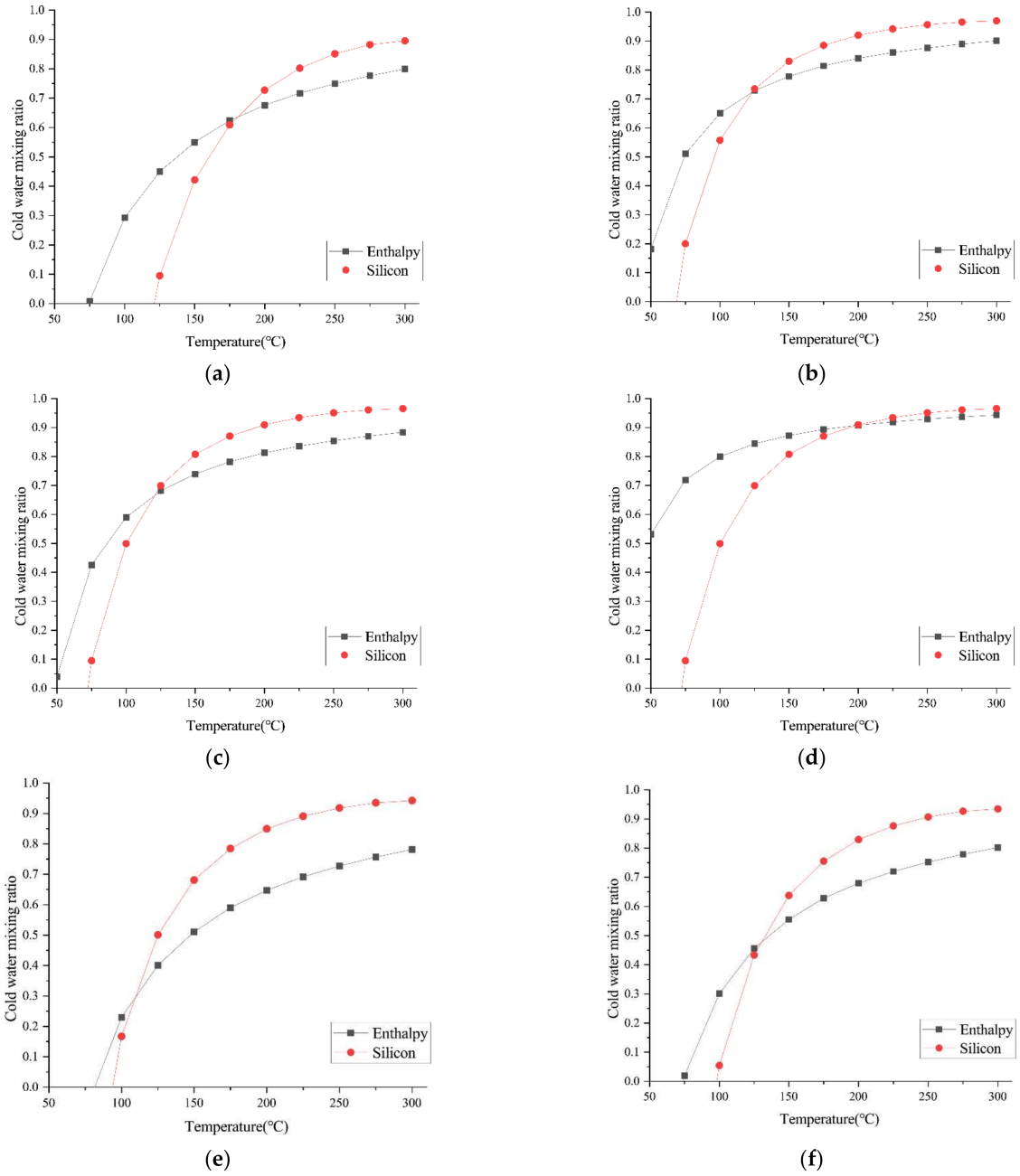

Figure 17. Si-enthalpy model of hot springs in the LFZ. (**a**) S04. (**b**) S16. (**c**) S08. (**d**) S13. (**e**) S14. (**f**) S19.

Zheng et al. [79] obtained that the deep geothermal reservoir temperature of Ganzi–Litang geothermal water is 71.92~105.14 °C, and the mixing ratio of cold water is 0.56~0.65 by chalcedony geothermometer and silicon-enthalpy model. However, reservoir temperatures obtained by quartz geothermometer in this paper are roughly consistent with the results from Zheng et al. [79]. The thermal reservoir temperature obtained by the silicon-enthalpy model is higher than from Zheng et al. [79], and the cation geothermometer is much higher. The hot spring cold water mixing ratio of LFZ is 0.32~0.89, and the ratio range is relatively wide. During the upwelling of underground geothermal water, it is constantly mixed with cold water. At different depths, the temperature of thermal water is extremely different. Therefore, with the increase in geothermal water, the temperature of water decreases. Different geothermometer calculate the different thermal reservoir temperature at a certain depth when a certain mineral is in an equilibrium state at that depth.

5.4. Spatial Distribution of Hydrogeochemical Characteristics in LFZ

As is shown in Figure 1, 13 hot springs are distributed among the three segments of the Litang fault system, and 6 hot springs are not distributed on the fault, but in the surrounding areas. Litang fault zone can be roughly divided into three segments: the northern margin fault of Maoyaba Basin, Litang fault, and Kangga–Dewu fault, which are called north segment, middle segment, and south segment, respectively. Overall, more hot springs and earthquakes are distributed in the middle segment. The hot springs in the northern, middle, and southern segments have moderate and high temperature. Among them, the high-temperature hot spring in the north segment of LFZ is the S04 hot spring, in the middle segment are the S09 and S14 hot springs, and in the south segment is the S19 hot spring. The long-term water temperature variation of S11~S13 hot spring in the middle segment of LFZ is in a wide range. When its temperature changes violently, it decreases sharply or rises sharply in a short time or continues to rise slowly, which indicates that there is a possibility of a $M > 7$ strong earthquake occurring in the Sichuan–Yunnan area [82]. S04 and S10 hot springs originated from the same thermal reservoir, and the circulation depth calculated from the present study are similar (see Figure 18), while the circulation depth of S17 hot spring in the south segment is relatively shallow. The hot springs heated by another heat source, except S14 hot spring, have medium circulation depths; however, S08 hot spring belongs to other heat sources, also has a medium circulation depth.

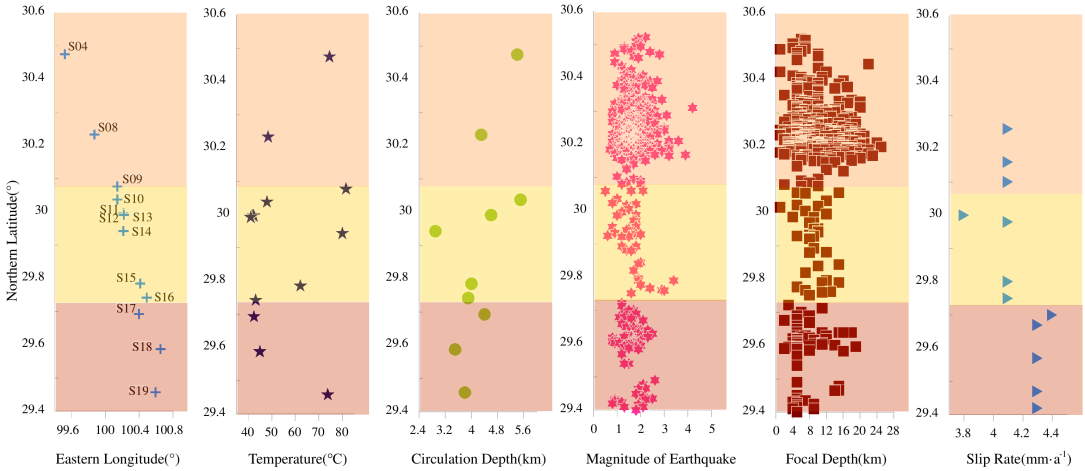

Figure 18. Spatial distribution of hydrogeochemical characteristics in the LFZ.

The Litang fault zone is an active fault zone with the ability to occur strong earthquakes, and the time of the last earthquake surface rupture of each segment of LFZ is different. The strong earthquake occurred 119 ± 2 a B.P. in the northern segment, the earthquakes occurred in the middle segment and southern segment are ~ 1890 AD and 1948 AD, respectively. As is shown in Figure 18, the earthquakes occurred in the LFZ are dominated by shallow

earthquakes, and the slip rates of the three segments are roughly the same. The seismic fracture has the characteristics of unidirectional migration from northwest to southeast, and there is strong interaction between the segments [28].

Earthquakes are more likely to occur in areas with deep groundwater circulation. The deeper the circulation is, the stronger the seismic activity is, indicating that underground fluid may be closely related to the seismogenic process. According to the small earthquakes observation catalogue since 2009, during the sampling period, the deeper the circulation depth is, the stronger the water–rock reaction is and the stronger the seismic activity is. When the groundwater circulation depth is deeper, the water seeping into the deep ground increases the pore fluid pressure, intensifies the liquid–rock reaction, weakens the fault zone, and is more prone to earthquakes [83]. Fluid circulation depth in the structural junction area is relatively deeper. The earthquakes tend to occur near the junction of the northern segment and the southern segment with the middle segment, respectively. Most of small earthquakes occurred in the northern segment, followed by the southern segment. The southern segment was ruptured in the 1948 M_s7.3 earthquake. The seismic activity in areas with deep geothermal water circulation deserves further attention.

5.5. Conceptual Model of Fluid Circulation

Geothermal water is recharged by the infiltrated precipitation and heated in fracture system by heat source during deep circulation process. Geothermal water is mainly controlled by deep faults in the LFZ. Hot springs are mostly exposed to the intersection region of branching faults and main faults, the upper wall of compressional fault or deep-incised valley formed by faulting. The 1890 M_s7.1 and 1948 M_s7.3 earthquakes occurred in Litang area resulted in some new springs in the Litanghe Valley [12]. Deep faults are not only conduits for further infiltration of groundwater, but also the conduits for upward flow of deep geothermal fluid. Hot springs in Litang area are recharged from the nearby mountainous areas, the recharge sources are meteoric water and glacier melting water. The recharge areas of hot springs are the high mountain areas in the west of Litang County, with the highest altitude of higher than 6000 m. Meteoric water and glacier melt water penetrate into aquifers through the hydraulic conductivity fracture zone between mountains and river terraces [84]. An obvious low velocity layer can be found at the depth of 15~35 km in Litang area, which shear wave velocity is lower than 3.2 km·s^{-1}. The velocity of S wave in the middle and lower crusts is relatively low, showing a large-scale low velocity trap. The upper boundary of the low-velocity zone is close to the depth of the Curie interface, about 17.2 km in Litang area. Low velocity trap in the middle and lower crust may be one of the deep heat sources in the hydrothermal activity area in western Sichuan [71]. Heat sources include the deep heat source connected by active faults, the heat source formed by magmatic sacs in the crust or volcanic magma, and the decay heat source of radioactive elements. The heat source that plays a major role in the formation of geothermal system in the region is the deep heat source linked by the Litang fault deep into the upper mantle, i.e., the deep mantle-derived magmatic heat and mechanical friction heat [85]. After infiltration recharge, groundwater flows along the tectonic fracture zone, or the contact zone between sedimentary rock and granite to the direction of Litanghe River, and circulates to the deep underground and converts into geothermal water. The application of ion thermometers requires cations to reach equilibrium state in thermal reservoir, and most of the hot springs in the Litang fault are immature water, so the depths of circulation given by ion thermometers are deeper, which can be considered as the upper limit of the depth of circulation. SiO_2 thermometer is appropriate for the case without cold water mixing. Therefore, the temperature of thermal reservoir considering cold water mixing is given in Section 5.3.3, and the depths of circulation of S04, S16, S08, S13, S14, and S19 hot springs are 3641 m, 2588 m, 2588 m, 4167 m, 2336 m, and 2715 m, respectively. The lower limit range of circulation depth of Litang fault hot spring is 2336~4167 m, and the upper limit range is 2504~5487 m. Hot springs in the Litang fault zone attribute to three different heat sources, belonging to three different geothermal systems. S08 hot spring has an independent heat

source of other hot springs and has a longer underground flow distance. In other hot springs, the flow direction along the Litang fault is roughly from northwest to southeast, and the S04, S10, and S17 constitute a runoff path. S09, S15, S13, S16, S18, S19, and S14 comprise another a flow path, which flows from S09 hot spring to S19 hot spring. After the groundwater reaches S15, it flows northward to Maoya where faults intersect, forming Maoya hot spring group, and then continues to flow southeastward among fault direction. After passing through the S16 and S18 to S19, the groundwater flow turns north again to reach the S14. When encountering a branch fault, the groundwater moves upward, mixes with shallow cold water and flows out of the surface to form a spring. Groundwater flow path in S14 hot spring is relatively long, but the ascending process is weak in mixed with cold water and still maintains high temperature. According to previous study on the gas geochemical characteristics of Litang fault, the majority of gas samples of the hot springs from the LFZ have discernible contributions of the mantle-derived He; however, S19 and S14 hot springs have significantly lower $^{3}He/^{4}He$ signatures, which indicates that these hot springs have longer transit time or flow paths [6]. To some extent, the circulation depth also indirectly reflects the difference of flow distance in the same geothermal water system.

As the conceptual model of ground fluid in the LFZ illustrated in Figure 19, when the groundwater infiltrates deep underground along fractures and faults, flows through the water–rock reaction zone, the underground fluid reacts with the surrounding rock. The deep circulating water strengthens the pore liquid pressure, strengthens the water–rock reaction, accelerates the surrounding rock weakening, and promotes the rock weakening of the fault zone to occur earthquakes. The stress accumulation before earthquakes can also open or close micro-cracks, thereby changing the permeability of aquifer. After earthquakes or before a strong earthquake, the stress state of underground medium changes, and the groundwater flow path will be changed, driving underground fluids to change circulation channels, result in water reacting with surrounding rock elsewhere. With the continuous accumulation of rock stress and the weakening of rock by water–rock reaction, earthquakes will occur in another place on the fault zone. The underground fluid movement may be work as the bridge among different segments in the fault zone.

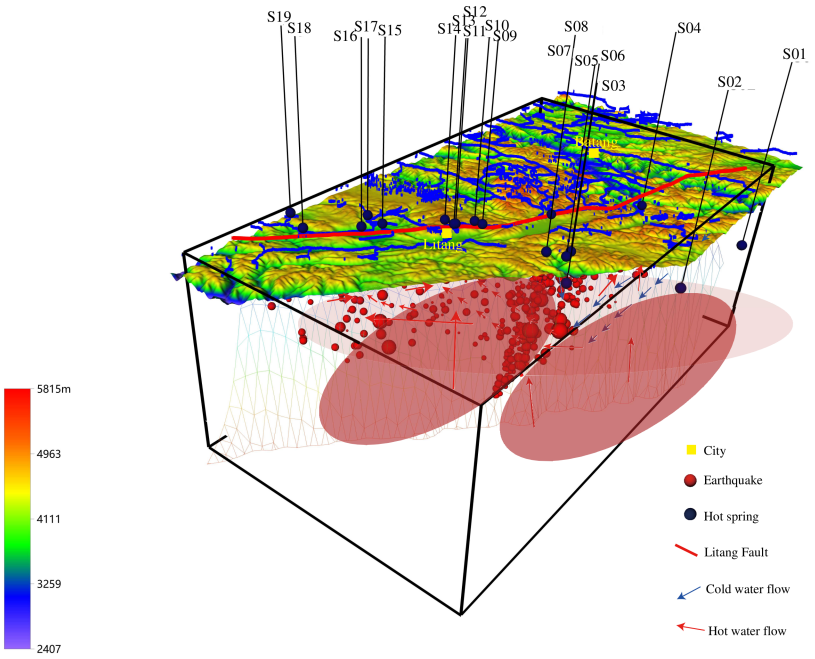

Figure 19. Conceptual model of ground fluid circulation in the LFZ.

6. Conclusions

Based on the observation of the geochemical characteristics of 19 hot springs in the Litang fault zone from 2010 to 2019, the conceptual model of ground fluid circulation in the LFZ is established, and the following conclusions can be drawn.

(1) The main hydrochemical type of hot spring water samples is HCO_3^--Na^+. The δ^2H values range from −157.6‰ to −123.4‰ and $\delta^{18}O$ values range from −24.5‰ to −15.4‰. Hot spring water in the Litang fault zone is mainly recharged by infiltrating precipitation, with recharge elevation of 4062~6018 m. The recharge area is mainly the high mountainous area in the west of Litang County.

(2) Hydrochemical types of Litang hot springs are mainly controlled by the circulation of groundwater in deep fault system, and is related to the rock lithology of thermal reservoir and water–rock reaction areas. Both CAI 1 and CAI 2 are negative values, indicating that reverse cation exchange has occurred in water samples collected from LFZ. Ca^{2+} and Mg^{2+} produced by carbonate rock dissolution in groundwater exchange with Na^+ and K^+ in the surrounding rock of the tunnel. The adsorption of Ca^{2+} and the release of Na^+ explain the increase in Na^+ in water samples, which will also lead to the change of chemical composition of water.

(3) Thermal reservoir temperatures of S04, S16, S08, S13, S14, and S19 hot springs are 175 °C, 125 °C, 125 °C, 200 °C, 113 °C, and 131 °C, respectively. The hot spring cold water mixing ratio of these hot springs is 0.32~0.89. The estimated lower limit range of circulation depth of the Litang fault hot spring is 2336~4167 m, and the upper limit range is 2504~5487 m.

(4) The hot springs in the Litang fault zone attribute to three different heat sources. The B/Li ratios of S09 and S15 hot springs are 4.51~7.64, S11~S13 hot springs are 6.50~7.04, S16 hot spring is 7.07~8.54, S18 and S19 hot springs are 8.11~9.86, and S14 hot spring is 13.33~15.12. It shows that groundwater flows roughly from north to south. It is worth noting that although S15 and S14 hot springs are concentrated in spatial location, the source of S14 hot spring may be shallower than other hot springs, and groundwater may flow a long distance before reaching S14 hot spring. The B/Li ratio of S04 hot spring is 2.26~2.55, which is the lowest ratio in the region. The B/Li ratio of S17 hot spring is 5.62~8.67, which has changed greatly in 2016 (8.67) compared with the samples collected in 2010 (5.90), 2017 (6.41), and 2018 (5.62). The B/Li ratio of S10 hot spring is 6.89~7.19. The groundwater flows roughly from north to south, when the flow reaches the position of S17 spring, and turns north. The B/Li ratio of S08 hot spring is 13.93~20.75, and the concentration of Cl^- is high, which may be from an independent reservoir source.

(5) The deeper the circulation depth of hot spring water on the fault, the higher the thermal reservoir temperature, the stronger the seismic activity of the segment, which is closely related to the increase in pore fluid pressure, rock weakening and deep fluid upwelling.

The study is helpful for further study on regional hydrogeological environment and provides a scientific basis for revealing geothermal fluid upwelling and movement in fault zone.

Supplementary Materials: The following supporting information can be downloaded at: https://www.mdpi.com/article/10.3390/w14091496/s1, Table S1: Results of field measured parameters, stable isotopes and concentrations of major ions in hot spring water samples in the Litang fault zone, Table S2: Trace elements in hot spring waters in LFZ, Table S3: Mineral saturation indices (SI) of hot springs in LFZ based on the PHREEQC database, Table S4: Mineral saturation indices (SI) of hot springs in LFZ based on the LLNL thermodynamic database, Table S5: Trace element of hot springs in the LFZ for enrichment factor calculation (μg/L), Table S6: The $^{87}Sr/^{86}Sr$ ratio in spring samples in the LFZ.

Author Contributions: Conceptualization, R.Z. and X.Z.; Data curation, J.D.; Formal analysis, R.Z.; Funding acquisition, R.Z. and X.Z.; Investigation, S.O. and F.L.; Methodology, Y.L. and K.L.; Resources, X.Z. and Z.L.; Software, M.H.; Supervision, Y.L.; Validation, X.Z., J.T., and Y.Y.; Visualization, J.L.; Writing—original draft, R.Z.; Writing—review and editing, X.Z. All authors have read and agreed to the published version of the manuscript.

Funding: The work was funded by Central Public-interest Scientific Institution Basal Research Fund (CEAIEF20220507, CEAIEF2022030205, CEAIEF20220213, CEAIEF2022050507), Beijing Natural Science Foundation (8224095), National Key Research and Development Project (2017YFC1500501-05, 2019YFC1509203), the National Natural Science Foundation of China (41673106, 42073063, 4193000170), and the Special Fund of the Institute of Earthquake Forecasting, China Earthquake Administration (2021IEF0101, 2021IEF0201, 2021IEF1201).

Institutional Review Board Statement: Not applicable.

Informed Consent Statement: Not applicable.

Data Availability Statement: The raw data supporting the conclusions of this article will be made available by the authors, without undue reservation.

Conflicts of Interest: The authors declare no conflict of interest.

References

1. Qiu, X.; Wang, Y.; Wang, Z.; Regenauer-Lieb, K.; Zhang, K.; Liu, J. Determining the origin, circulation path and residence time of geothermal groundwater using multiple isotopic techniques in the Heyuan Fault Zone of Southern China. *J. Hydrol.* **2018**, *567*, 339–350. [CrossRef]
2. Blomgren, V.J.; Crossey, L.J.; Karlstrom, K.E.; Fischer, T.P.; Darrah, T.H. Hot spring hydrochemistry of the Rio Grande rift in northern New Mexico reveals a distal geochemical connection between Valles Caldera and Ojo Caliente. *J. Volcanol. Geoth. Res.* **2019**, *387*, 106663. [CrossRef]
3. Hu, S.; He, L.; Wang, J. Heat flow in the continental area of China: A new data set. *Earth Planet. Sci. Lett.* **2000**, *179*, 407–419. [CrossRef]
4. Tang, H.H.; Guo, L.H.; Fang, Y. Estimation of heat slow in southeastern margin of Tibetan Plateau and its analysis of the correlation with earthquake activity. *Chinese J. Geophys.* **2020**, *63*, 1056–1069. (In Chinese)
5. Shi, Z.; Liao, F.; Wang, G.; Xu, Q.; Mu, W. Hydrogeochemical characteristics and evolution of hot springs in eastern Tibetan Plateau Geothermal Belt, Western China: Insight from multivariate statistical analysis. *Geofluids* **2017**, 6546014. [CrossRef]
6. Zhou, X.; Liu, L.; Chen, Z.; Cui, Y.; Du, J. Gas geochemistry of the hot spring in the Litang fault zone, Southeast Tibetan Plateau. *Appl. Geochem.* **2017**, *79*, 17–26. [CrossRef]
7. Hou, Y.; Shi, Z.; Mu, W. Fluid geochemistry of fault zone hydrothermal system in the Yidun-Litang Area, Eastern Tibetan Plateau Geothermal Belt. *Geofluids* **2018**, 6872563. [CrossRef]
8. Li, J.; Sagoe, G.; Yang, G.; Liu, D.; Li, Y. The application of geochemistry to bicarbonate thermal springs with high reservoir temperature: A case study of the Batang geothermal field, western Sichuan Province, China. *J. Volcanol. Geoth. Res.* **2019**, *371*, 20–31. [CrossRef]
9. Chen, Z.; Zhou, X.; Du, J.; Xie, C.; Liu, L.; Li, Y.; Liu, H.; Cui, Y. Hydrochemical characteristics of hot spring waters in the Kangding district related to the Lushan M_S = 7.0 earthquake in Sichuan, China. *Nat. Hazards Earth Syst. Sci.* **2015**, *15*, 1149–1156. [CrossRef]
10. Li, B.; Shi, Z.; Wang, G.; Liu, C. Earthquake-related hydrochemical changes in thermal springs in the Xianshuihe Fault zone, Western China. *J. Hydrol.* **2019**, *579*, 124175. [CrossRef]
11. Tang, X.; Zhang, J.; Pang, Z.; Hu, S.; Tian, J.; Bao, S. The eastern Tibetan Plateau geothermal belt, western China: Geology, geophysics, genesis, and hydrothermal system. *Tectonophysics* **2017**, *717*, 433–448. [CrossRef]
12. Zhang, J.; Li, W.Y.; Tang, X.C.; Tian, J.; Wang, Y.C.; Guo, Q.; Pang, Z.H. Geothermal data analysis at the high-temperature hydrothermal area in Western Sichuan. *Sci. China Earth Sci.* **2017**, *60*, 1507–1521. [CrossRef]
13. Chevalier, M.-L.; Leloup, P.H.; Replumaz, A.; Pan, J.; Liu, D.; Li, H.; Gourbet, L.; Métois, M. Tectonic-geomorphology of the Litang fault system, SE Tibetan Plateau, and implication for regional seismic hazard. *Tectonophysics* **2016**, *682*, 278–292. [CrossRef]
14. Deng, Q.; Zhang, P.; Ran, Y.; Yang, X.; Min, W.; Chu, Q. Basic characteristics of active tectonics of China. *Sci. China Ser. D Earth Sci.* **2003**, *46*, 356–372.
15. Zhang, P. A review on active tectonics and deep crustal processes of the Western Sichuan region, eastern margin of the Tibetan Plateau. *Tectonophysics* **2016**, *584*, 7–22. [CrossRef]
16. Reid, A.J.; Wilson, C.J.L.; Liu, S. Structural evidence for the Permo-Triassic tectonic evolution of the Yidun Arc, eastern Tibetan Plateau. *J. Struct. Geol.* **2005**, *27*, 119–137. [CrossRef]
17. Liu, S., Jr.; Jackson, W.T.; Robinson, D.M.; Weislogel, A.L.; Jian, X. Cenozoic reactivation along the Late Triassic Ganzi-Litang suture, eastern Tibetan Plateau. *Geosci. Front.* **2020**, *11*, 1069–1080. [CrossRef]

18. Yu, H.J.; Jiang, J.W.; Li, W.C. Controls of variable crustal thicknesses on Late Triassic mineralization in the Yidun Arc, Eastern Tibet. *J. Asian Earth Sci.* **2020**, *195*, 104285. [CrossRef]
19. Wang, B.Q.; Wang, W.; Zhou, M. Provenance and tectonic setting of the Triassic Yidun Group, the Yidun Terrane, Tibet. *Geosci. Front.* **2013**, *4*, 765–777. [CrossRef]
20. Li, W.C.; Yu, H.J.; Gao, X.; Liu, X.L.; Wang, J.H. Review of Mesozoic multiple magmatism and porphyry Cu–Mo (W) mineralization in the Yidun Arc, eastern Tibet Plateau. *Ore Geol. Rev.* **2017**, *90*, 795–812. [CrossRef]
21. Xu, B.; Hou, Z.Q.; Griffin, W.L.; Zheng, Y.C.; Wang, T.; Guo, Z.; Hou, J.; Santosh, M.; O'Reilly, S.Y. Cenozoic lithospheric architecture and metallogenesis in Southeastern Tibet. *Earth-Sci. Rev.* **2021**, *214*, 103472. [CrossRef]
22. Zhu, D.C.; Wang, Q.; Zhan, Q.Y.; Xie, J.C. Late Triassic tectonomagmatism of northern Sanjiang and associated several scientific problems. *Sediment. Geol. Tethyan Geol.* **2021**. in press (In Chinese)
23. Wu, T.; Xiao, L.; Wilde, S.A.; Ma, C.Q.; Li, Z.L.; Sun, Y.; Zhan, Q.Y. Zircon U–Pb age and Sr–Nd–Hf isotope geochemistry of the Ganluogou dioritic complex in the northern Triassic Yidun arc belt, Eastern Tibetan Plateau: Implications for the closure of the Garzê-Litang Ocean. *Lithos* **2016**, *248–251*, 94–108. [CrossRef]
24. Wu, T.; Xiao, L.; Wilde, S.A.; Ma, C.Q.; Zhou, J.X. A mixed source for the Late Triassic Garzê-Daocheng granitic belt and its implications for the tectonic evolution of the Yidun arc belt, eastern Tibetan Plateau. *Lithos* **2017**, *288–289*, 214–230. [CrossRef]
25. Gao, X.; Yang, L.Q.; Orovan, E.A. The lithospheric architecture of two subterranes in the eastern Yidun Terrane, East Tethys: Insights from Hf–Nd isotopic mapping. *Gondwana Res.* **2018**, *62*, 127–143. [CrossRef]
26. Zhan, Q.Y.; Zhu, D.C.; Wang, Q.; Cawood, P.A.; Xie, J.C.; Liu, X.; Li, S.M.; Zhang, L.L.; Zhao, Z.D. Imaging the Late Triassic lithospheric architecture of the Yidun Terrane, eastern Tibetan Plateau: Observations and interpretations. *Geol. Soc. Am. Bull.* **2021**, *133*, 2279–2290. [CrossRef]
27. Gong, X.; Yang, Z.; Meng, X.; Pan, X.; Wang, Q.; Zhang, L. Late Paleozoic to Mesozoic intrusions distribution in the north Sanjiang Orogenic Belt, Southwest China: Evidence from zircon U–Pb dating and geochemistry. *Acta Geol. Sin. (Engl. Ed.)* **2017**, *91*, 898–946. [CrossRef]
28. Xu, X.; Wen, X.; Yu, G.; Zheng, R.; Luo, H.; Zheng, B. Average slip rate, earthquake rupturing segmentation and recurrence behavior on the Litang fault zone, western Sichuan Province, China. *Sci. China Ser. D Earth Sci.* **2005**, *48*, 1183–1196. [CrossRef]
29. Zhang, Y.-Z.; Replumaz, A.; Wang, G.C.; Leloup, P.H.; Gautheron, C.; Bernet, M.; van der Beek, P.; Paquette, J.L.; Wang, A.; Zhang, K.-X.; et al. Timing and rate of exhumation along the Litang fault system, implication for fault reorganization in Southeast Tibet. *Tectonics* **2015**, *34*, 1219–1243. [CrossRef]
30. Molenda, T. Impact of saline mine water: Development of a meromictic reservoir in Poland. *Mine Water Environ.* **2014**, *33*, 327–334. [CrossRef]
31. Woith, H.; Wang, R.; Maiwald, U.; Pekdeger, A.; Zschau, J. On the origin of geochemical anomalies in groundwaters induced by the Adana 1998 earthquake. *Chem. Geol.* **2013**, *339*, 177–186. [CrossRef]
32. Bian, Y.; Zhao, D. Genesis of geothermal waters in the Kangding geothermal field, Sichuan Province. *Acta Geosci. Sin.* **2018**, *39*, 491–497. (In Chinese)
33. Kurdi, M.; Hezarkhani, R.; Eslamkish, T. Assessment of chemical properties and hydro-geochemical coefficients at the Qareh Sou Basin, Golestan Province, Iran. *Environ. Earth Sci.* **2014**, *72*, 3243–3249. [CrossRef]
34. Craig, H. Isotopic variations in meteoric waters. *Science* **1961**, *133*, 1702–1703. [CrossRef]
35. Li, L.; Garzione, G.N. Spatial distribution and controlling factors of stable isotopes in meteoric waters on the Tibetan Plateau: Implications for paleoelevation reconstruction. *Earth Planet Sc. Lett.* **2017**, *460*, 302–314. [CrossRef]
36. Giggenbach, W.F. Isotopic shifts in waters from geothermal and volcanic systems along convergent plate boundaries and their origin. *Earth Planet Sc. Lett.* **1992**, *113*, 495–510. [CrossRef]
37. Ma, Z.; Yu, J.; Su, Y.; Xie, J.; Jia, X.; Hu, Y. δ^{18}O shifts of geothermal waters in the central of Weihe Basin, NW China. *Environ. Earth Sci.* **2010**, *59*, 995–1008. [CrossRef]
38. Jeelani, G.; Kumar, U.S.; Kumar, B. Variation of δ^{18}O and δD in precipitation and stream waters across the Kashmir Himalaya (India) to distinguish and estimate the seasonal sources of stream flow. *J. Hydrol.* **2013**, *481*, 157–165. [CrossRef]
39. Blash, K.W.; Bryson, J.R. Distinguishing sources of ground water recharge by using delta2H and delta18O. *Ground Water* **2007**, *45*, 294–308. [CrossRef]
40. Bowen, G.J.; Wilkinson, B. Spatial distribution of δ^{18}O in meteoric precipitation. *Geology* **2002**, *30*, 315–318. [CrossRef]
41. Bowen, G.J.; Revenaugh, J. Interpolating the isotopic composition of modern meteroric precipitation. *Water Resour. Res.* **2003**, *39*, 1–13. [CrossRef]
42. Feng, S.; Liu, X.; Li, H. Spatial variation of δD and δO in lake water of western China and their controlling factors. *J. Lake Sci.* **2020**, *32*, 1199–1211. (In Chinese)
43. Yang, X.X.; Xu, B.Q.; Yang, W.; Qu, D.M. The Indian monsoonal influence on altitude effect of δ^{18}O in surface water on southeast Tibetan Plateau. *Sci. China: Earth Sci.* **2012**, *55*, 438–445. [CrossRef]
44. Sidkina, E.S. Brines in the western part of the Tunguska Artesian Basin. *Geochem. Int.* **2015**, *53*, 735–747. [CrossRef]
45. Piper, A.M. A graphic procedure in the geochemical interpretation of water-analyses. *EOS, Trans., Am. Geophys. Union* **1944**, *25*, 914–928. [CrossRef]
46. Zhao, J.; Wang, G.; Zhang, C.; Xing, L.; Li, M.; Zhang, W. Genesis of geothermal fluid in typical geothermal fields in Western Sichuan, China. *Acta Geol. Sin. (Engl. Ed.)* **2021**, *95*, 873–882. [CrossRef]

47. Apollaro, C.; Vespasiano, G.; De Rosa, R.; Marini, L. Use of mean residence time and flowrate of thermal waters to evaluate the volume of reservoir water contributing to the natural discharge and the related geothermal reservoir volume. Application to Northern Thailand hot springs. *Geothermics* **2015**, *58*, 62–74. [CrossRef]
48. Apollaro, C.; Vespasiano, G.; Muto, F.; De Rosa, R.; Barca, D.; Marini, L. Use of mean residence time of water, flowrate, and equilibrium temperature indicated by water geothermometers to rank geothermal resources. Application to the thermal water circuits of Northern Calabria. *J. Volcanol. Geotherm. Res.* **2016**, *328*, 147–158. [CrossRef]
49. Zhao, J.; Zhang, W.; Zhang, H.; Qu, Z.; Li, M.; Yue, G. Hydrogeochemical characteristics and genesis of the geothermal fields in Batang of Sichuan. *Hydrogeol. Eng. Geol.* **2019**, *46*, 81–89. (In Chinese)
50. Peng, C.; Liu, Y.; Chen, H.; Yuan, Q.; Chen, Q.; Mei, S.; Wu, Z. Analysis of hydrogeochemical characteristics of tunnel groundwater based on multivariate statistical technology. *Geofluids* **2021**, *2021*, 4867942. [CrossRef]
51. Long, D.; Huang, F.; Guan, Z. Analysis on the geotectonic environment and the forming factors of the hot spring in Maoya. *Earthquake Res. Sichuan* **2006**, *118*, 34–40. (In Chinese)
52. Martínez-Florentino, T.A.K.; Esteller-Alberich, M.V.; Expósito, J.L.; Domínguez-Mariani, E.; Morales-Arredondo, J.I. Hydrogeochemistry and geothermometry of thermal springs in the eastern Trans-Mexican Volcanic Belt. *Geothermics* **2021**, *96*, 102176. [CrossRef]
53. Apollaro, C.; Caracausi, A.; Paternoster, M.; Randazzo, P.; Aiuppa, A.; De Rosa, R.; Fuoco, I.; Mongelli, G.; Muto, F.; Vanni, E.; et al. Fluid geochemistry in a low-enthalpy geothermal field along a sector of southern Apennines chain (Italy). *J. Geochem. Explor.* **2020**, *219*, 106618. [CrossRef]
54. Frondini, F. Geochemistry of regional aquifer systems hosted by carbonate-evaporite formations in Umbria and southern Tuscany (central Italy). *Appl. Geochem.* **2008**, *23*, 2091–2104. [CrossRef]
55. Nicholson, K. *Geothermal Fluids: Chemistry and Exploration Techniques*; Springer: Berlin/Heidelberg, Germany; pp. 1–263.
56. Kanduč, T.; Mori, N.; Kocman, D.; Stibilj, V.; Grassa, F. Hydrogeochemistry of Alpine springs from North Slovenia: Insights from stable isotopes. *Chem. Geol.* **2012**, *300-301*, 40–54. [CrossRef]
57. Wang, B.Q.; Zhou, M.F.; Chen, W.T.; Gao, J.F.; Yan, D.P. Petrogenesis and tectonic implications of the Triassic volcanic rocks in the northern Yidun Terrane, Eastern Tibet. *Lithos* **2013**, *175-176*, 285–301. [CrossRef]
58. Wang, B.; Zhou, X.; Zhou, Y.; Yan, Y.; Ouyang, S.; Liu, F.; Zhong, J. Hydrogeochemistry and precursory anomalies in thermal springs of Fujian (Southeastern China) associated with earthquakes in the Taiwan Strait. *Water* **2021**, *13*, 3523. [CrossRef]
59. Chao, H.C.; You, C.F.; Liu, H.C.; Chung, C.H. Evidence for stable Sr isotope fractionation by silicate weathering in a small sedimentary watershed in southwestern Taiwan. *Geochim. Cosmochim. Acta* **2015**, *165*, 324–341. [CrossRef]
60. Capo, R.C.; Stewart, B.W.; Chadwick, O.A. Strontium isotopes as tracers of ecosystem processes: Theory and methods. *Geoderma* **1998**, *82*, 197–225. [CrossRef]
61. Hajj, F.; Poszwa, A.; Bouchez, J.; Guerold, F. Radiogenic and "stable" strontium isotopes in provenance studies: A review and first results on archaeological wood from shipwrecks. *J. Archaeol. Sci.* **2017**, *86*, 24–49. [CrossRef]
62. Zhang, Z. $^{87}Sr/^{86}Sr$ data for some middle-late Proterozoic to early Cambrian carbonate rocks in China. *Geol. Rev.* **1995**, *41*, 349–354. (In Chinese)
63. Tian, J.; Pang, Z.; Wang, Y.; Guo, Q. Fluid geochemistry of the Cuopu high temperature geothermal system in the eastern Himalayan syntaxis with implication on its genesis. *Environ. Appl. Geochem.* **2019**, *110*, 104422. [CrossRef]
64. Tian, J.; Pang, Z.; Liao, D.; Zhou, X. Fluid geochemistry and its implications on the role of deep faults in the genesis of high temperature systems in the eastern edge of the Qinghai Tibet Plateau. *Environ. Appl. Geochem.* **2021**, *131*, 105036. [CrossRef]
65. Harrington, G.A.; Herczeg, A.L. The importance of silicate weathering of a sedimentary aquifer in arid Central Australia indicated by very high $^{87}Sr/^{86}Sr$ ratios. *Chem. Geol.* **2003**, *199*, 281–292. [CrossRef]
66. Dai, Z.; Sun, C. Sedimentary facies and paleogeography of the Upper Triassic Qugasi Formation in Yidun, Sichuan. *Acta Geol. Sichuan* **2008**, *28*, 266–271. (In Chinese)
67. Wang, X.; Tang, Z. The first large-scale bioavailable Sr isotope map of China and its implication for provenance studies. *Earth-Sci. Rev.* **2020**, *210*, 103353. [CrossRef]
68. Giggenbach, W.F. Geothermal solute equilibria. Derivation of Na-K-Mg-Ca geoindicators. *Geochim. Cosmochim. Acta* **1988**, *52*, 2749–2765. [CrossRef]
69. Romano, P.; Liotta, M. Using and abusing Giggenbach ternary Na-K-Mg diagram. *Chem. Geol.* **2020**, *541*, 119577. [CrossRef]
70. Guo, Q.; Pang, Z.; Wang, Y.; Tian, J. Fluid geochemistry and geothermometry applications of the Kangding high-temperature geothermal system in eastern Himalayas. *Appl. Geochem.* **2017**, *81*, 63–75. [CrossRef]
71. Li, W.Y.; Zhang, J.; Tang, X.C.; Tian, J.; Wang, Y.C.; Guo, Q. The deep geothermal structure of high-temperature hydrothermal activity region in western Sichuan Plateau: A geophysical study. *Chinese J. Geophys.* **2018**, *61*, 2926–2936. (In Chinese)
72. Fournier, R.O. Chemical geothermometers and mixing models for geothermal systems. *Geothermics* **1977**, *5*, 41–50. [CrossRef]
73. Kharaka, Y.K.; Lico, M.S.; Lawl, L.M. Chemical geothermometers applied to formation waters, Gulf of Mexico and California basins: ABSTRACT. *Am. Assoc. Pet. Geol. Bull.* **1982**, *66*, 588–589.
74. Kharaka, Y.K.; Mariner, R.H. Chemical geothermometers and their application to formation waters from sedimentary basins. In *Thermal History of Sedimentary Basins*; Naeser, N.D., McCulloh, T.H., Eds.; Springer: New York, NY, USA, 1989; pp. 99–117.
75. Fournier, R.O.; Truesdell, A.H. An empirical Na-K-Ca geothermometer for natural waters. *Geochim. Cosmochim. Acta* **1973**, *37*, 1255–1275. [CrossRef]

76. Wang, J.; Jin, M.; Jia, B.; Kang, F. Hydrochemical characteristics and geothermometry applications of thermal groundwater in northern Jinan, Shandong, China. *Geothermics* **2015**, *57*, 185–195. [CrossRef]
77. Chiodini, G.; Frondini, F.; Marini, L. Theoretical geothermometers and P_{CO_2} indicators for aqueous solutions coming from hydrothermal systems of medium-low temperature hosted in carbonate-evaporite rocks. Application to the thermal springs of the Etruscan Swell, Italy. *Appl. Geochem.* **1995**, *10*, 337–346.
78. Minissale, A.A.; Duchi, D. Geothermometry on fluids circulating in a carbonate reservoir in North-Centre Italy. *J. Volcanol. Geoth. Res.* **1988**, *35*, 237–252.
79. Zhang, W.; Wang, G.; Zhao, J.; Liu, F. Geochemical characteristics of medium-high temperature geothermal fluids in West Sichuan and their geological implications. *Geoscience* **2021**, *35*, 188–198. (In Chinese)
80. Reed, M.; Spycher, N. Calculation of pH and mineral equilibria in hydrothermal waters with application to geothermometry and studies of boiling and dilution. *Geochim. Cosmochim. Acta* **1984**, *48*, 1479–1492.
81. Huang, X.; Sillanpää, M.; Gjessing, E.T.; Vogt, R.D. Water quality in the Tibetan Plateau: Major ions and trace elements in the headwaters of four major Asian rivers. *Sci. Total Environ.* **2009**, *407*, 6242–6254.
82. Li, J.; Huang, S.; Wen, X. Discussing the temperature abnormal changes of spring water in Maoya. *Acta Geol. Sichuan* **2005**, *25*, 10–16. (In Chinese)
83. Wintsch, R.P.; Christoffersen, R.; Kronenberg, A.K. Fluid-rock reaction weakening of fault zones. *J. Geophys. Res.: Solid Earth* **1995**, *100*, 13021–13032.
84. Yan, Y.; Zhou, X.; Liao, L.; Tian, J.; Li, Y.; Shi, Z.; Liu, F.; Ouyang, S. Hydrogeochemical characteristic of geothermal water and precursory anomalies along the Xianshuihe Fault Zone, Southwestern China. *Water* **2022**, *14*, 550.
85. Wei, Y.; Hu, Y. Formation of the hot springs in Kahui, Litang, Sichuan. *J. Geol. Hazards Environ. Preserv.* **2014**, *25*, 78–82. (In Chinese)